

Gravitational collapse and the thermal evolution of low-metallicity gas clouds in the early Universe

Gen Chiaki,^{1,2*} Naoki Yoshida^{1,3} and Shingo Hirano^{1,4}

¹*Department of Physics, Graduate School of Science, University of Tokyo, 7-3-1 Hongo, Bunkyo, Tokyo 113-0033, Japan*

²*Department of Physics, Konan University, 8-9-1 Okamoto, Kobe, 658-0072, Japan*

³*Kavli Institute for the Physics and Mathematics of the Universe (WPI), Todai Institutes for Advanced Study, The University of Tokyo, Kashiwa, Chiba 277-8583, Japan*

⁴*Department of Astronomy, The University of Texas, Austin, TX 78712, USA*

ABSTRACT

We study gravitational collapse of low-metallicity gas clouds and the formation of protostars by three-dimensional hydrodynamic simulations. Grain growth, non-equilibrium chemistry, molecular cooling, and chemical heating are solved in a self-consistent manner for the first time. We employ the realistic initial conditions for the abundances of metal and dust, and the dust size distribution obtained from recent Population III supernova calculations. We also introduce the state-of-the-art particle splitting method based on the Voronoi tessellation and achieve an extremely high mass resolution of $\sim 10^{-5} M_{\odot}$ (10 Earth masses) in the central region. We follow the thermal evolution of several clouds with various metallicities. We show that the condition for cloud fragmentation depends not only on the gas metallicity but also on the collapse timescale. In many cases, the cloud fragmentation is prevented by the chemical heating owing to molecular hydrogen formation even though dust cooling becomes effective. Meanwhile, in several cases, efficient OH and H₂O cooling promotes the cloud elongation, and then cloud “filamentation” is driven by dust thermal emission as a precursor of eventual fragmentation. While the filament fragmentation is driven by rapid gas cooling with metallicity $\gtrsim 10^{-5} Z_{\odot}$, fragmentation occurs in a different manner by the self-gravity of a circumstellar disk with metallicity $\lesssim 10^{-5} Z_{\odot}$. We use a semi-analytic model to estimate the number fraction of the clouds which undergo the filament fragmentation to be 20–40% with metallicity 10^{-5} – $10^{-4} Z_{\odot}$. Overall, our simulations show a viable formation path of the recently discovered Galactic low-mass stars with extremely small metallicities.

Key words: dust, extinction — galaxies: evolution — ISM: abundances — stars: formation — stars: low-mass — stars: Population II

1 INTRODUCTION

The origin of Galactic extremely metal-poor (EMP) stars remains largely unknown. Their small metal content suggests that they were born very early, while their small masses pose interesting questions on star formation in a metal-poor environment. For example, the star SDSS J102915 + 172927 with a mass $0.8 M_{\odot}$ has an extremely low metallicity of $4.5 \times 10^{-5} Z_{\odot}$ (Caffau et al. 2011b, 2012), and thus is thought to be a second generation star; it was probably born in a gas cloud that had been enriched with heavy elements synthesized by the first generation of stars (Pop III stars).

Recent theoretical studies based on cosmological hydrodynamic simulations suggest that the first generation

stars formed from a metal-free, primordial gas have a wide range of masses (Hirano et al. 2014; Susa et al. 2014). Such a notion is supported by observations of EMP stars whose peculiar abundance patterns are consistent with the nucleosynthetic models of massive primordial stars (Caffau et al. 2011b; Keller et al. 2014). Interestingly, the recently discovered star SDSS J001820.5 – 093939.2 shows characteristic signatures of the metal yield of a very massive primordial star, suggesting a broad mass distribution of Pop III stars (Aoki et al. 2014). In addition, it is reported that the fragmentation of accretion disk in the primordial gas clouds leads the solar- and subsolar-mass star formation when clumps are ejected from the dense region by the N -body gravitational interactions (Greif et al. 2011, 2012; Clark et al. 2011; Stacy & Bromm 2014). If their mass is less than $\sim 1 M_{\odot}$, these stars might be observed in the

* E-mail: chiaki@center.konan-u.ac.jp

local Universe (Hartwig et al. 2015; Ishiyama et al. 2016), and the slightly polluted Pop III stars might be observed as metal-poor stars (Komiya et al. 2015).

A trace amount of heavy elements in star-forming gas plays an important role in the formation of low-mass stars with extremely low metallicities (Omukai 2000; Bromm & Loeb 2003; Schneider et al. 2003). Efficient gas cooling from metal and dust can trigger the cloud fragmentation. In general, gas cooling promotes cloud deformation into sheets or filaments, whereas heating processes stabilize the gas against aspherical perturbations. Linear analyses by Lai (2000) and Hanawa & Matsumoto (2000) demonstrate that a contracting cloud gets highly elongated when the specific heat ratio $\gamma = d \ln T / d \ln \rho + 1$, an indicator of the effective gas equation of state, is less than 1.1. In a cooling gas with $\gamma < 1$, significantly elongated filamentary structures tend to form. When the density of the filament increases up to a value where gas cooling becomes insufficient ($\gamma > 1$), multiple cores are formed and begin contracting separately. Therefore, the characteristic mass of the fragments is set by the Jeans mass at the density and temperature where the cooling becomes inefficient.

Analytic models and simulations suggest that intermediate-mass cores ($\sim 100 M_{\odot}$) are formed by transition line cooling of C I, C II, and O I (Bromm & Loeb 2003; Frebel et al. 2005; Santoro & Shull 2006; Safranek-Shrader et al. 2014a). Low-mass stars might be formed by the dynamical ejection with N -body interactions among these clumps (Ji et al. 2014). Dust thermal emission is another important process that determines the thermal evolution of a low-metallicity gas. A semi-analytic approach reveals that dust cooling becomes important at densities $n_{\text{H}} \gtrsim 10^{12} \text{ cm}^{-3}$, where the corresponding Jeans mass is $\sim 0.1 M_{\odot}$ (Omukai 2000; Schneider et al. 2003).

Three-dimensional hydrodynamic simulations also have been performed to study the conditions for gas cloud fragmentation and for the formation of low-mass stars. Jappsen et al. (2007, 2009a,b) investigate the process of low-metal gas collapse with a wide range of parameter set. They find that gas metallicity has little effect on cloud evolution and fragmentation even with metallicities around $10^{-3} Z_{\odot}$ in the earlier stage of collapse ($n_{\text{H}} < 10^5 \text{ cm}^{-3}$) in fossile H II region created by a Pop III star. Rather, the other parameter such as Dopcke et al. (2011, 2013) follow the dynamical evolution of a turbulent gas with metallicities below $10^{-4} Z_{\odot}$. They show that several tens of sink particles are formed in the gas and that the mass distribution of the sink particles transitions from flat to peaky distribution with increasing metallicity. Safranek-Shrader et al. (2014a,b) perform simulations with a proper cosmological setup to investigate star formation in dense clumps in early galaxies with gas metallicities of 10^{-4} – $10^{-2} Z_{\odot}$. Safranek-Shrader et al. (2014b) find that, with metallicity $10^{-2} Z_{\odot}$, the gas fragments into sink particles, whose mass distribution is consistent with observationally derived stellar masses in ultra faint dwarf spheroidal galaxies as observed by Geha et al. (2013). More recently, Safranek-Shrader et al. (2016) resume simulations with an updated protostar model, and find that the mass distribution of sink particles resembles the Salpeter mass function. Smith et al. (2015) study the effects of metal pollution and turbulence driven by a Pop III supernova (SN) explosion on a neighboring halo. The gas polluted to metal-

licity of $2 \times 10^{-5} Z_{\odot}$ fragments by dust thermal emission. Their study explicitly includes the process of the dispersion of metals and dust.

These previous studies assume the metal abundances, grain condensation efficiency, and the dust size distribution to be those in the Galactic interstellar medium despite the fact that the EMP stars observed so far show peculiar abundance patterns (also see the recently submitted paper of Bovino et al. 2016). For example, the abundance ratio of light elements, such as carbon and oxygen relative to iron is enhanced with respect to the solar value (Suda et al. 2008; Tominaga et al. 2014). Because the efficiency of metal line cooling is determined by the abundance of individual elements, it is important to adopt realistic values based on, for example, the nucleosynthesis calculations of Pop III SNe.

The same is true for the condensation efficiency, or the mass fraction of heavy elements condensed into dust grains. It is known that a significant fraction of heavy elements are locked into dust grains in the local interstellar medium (Pollack et al. 1994), but recent spectroscopic observations of damped Lyman- α systems with metallicity $\sim 10^{-3} Z_{\odot}$ suggest that the condensation efficiency is smaller at redshifts $z \sim 6$ (Schady et al. 2010; Zafar et al. 2011). It is also known that grain growth, i.e., accretion of the gas-phase metals onto dust grains, can enhance the dust cooling efficiency in a collapsing cloud even with an extremely low metallicity to be close to that of the local interstellar medium (Nozawa et al. 2012; Chiaki et al. 2013).

There are other important processes in low-metallicity gas that have often been overlooked in previous studies. O-bearing molecules such as OH and H₂O act as important coolants at intermediate densities $n_{\text{H}} \sim 10^4$ – 10^8 cm^{-3} . Although OH and H₂O cooling is less effective in a gas with a solar composition (Jappsen et al. 2007; Omukai 2000), our previous work (Chiaki et al. 2015, hereafter C15) reveals that the molecular cooling is efficient in some cases when the realistic initial condition (composition) is adopted. There is yet another important heating process. When hydrogen molecules are formed, the binding energy is released to be converted into the gas kinetic energy. Tsuribe & Omukai (2008) argue that this gas heating can stabilize the gas to prevent fragmentation using simulations of a polytropic gas mimicking the thermal evolution of low-metallicity clouds.

Metal and dust properties in the early Universe can be determined theoretically under the assumption that the formation sites of low-metallicity stars are in clouds partly polluted with metals and dust by Pop III SNe in the same or nearby halos (Ritter et al. 2012; Smith et al. 2015). Thus, the abundances of heavy elements and dust species, and the dust size distribution are expected to be set by nucleosynthetic process in SN explosion (Umeda & Nomoto 2002) and the dust formation and destruction history during the propagation of blast waves (Todini & Ferrara 2001; Nozawa et al. 2003; Schneider et al. 2006).

In this work, we perform hydrodynamic simulations of collapsing gas clouds with various metallicities 10^{-6} – $10^{-3} Z_{\odot}$. We study in detail the critical conditions for gas fragmentation and for the formation of low-mass protostars. Our three-dimensional simulations follow, for the first time, all the necessary thermal processes including dust thermal emission, gas heating by H₂ formation, and OH and H₂O cooling. The metal abundances, initial grain condensation

efficiency, and the dust size distribution are calculated from stellar evolution and SN explosion models of a Pop III star with $30 M_{\odot}$. We calculate the chemical reactions and grain growth in a direct, self-consistent manner in order to compute the cooling and heating rates. Recently, Hirano et al. (2014) find that the different collapse timescales of the primordial star-forming cloud gives the wide mass distribution of Pop III stars, $\sim 10\text{--}1000 M_{\odot}$. In this paper, we employ four gas clouds with different collapse timescales to examine the effect of the cloud variation on low-metallicity star formation.

2 NUMERICAL SIMULATIONS

2.1 Chemistry and cooling

We use the parallel N -body/smoothed particle hydrodynamics (SPH) code GADGET-2 (Springel 2005) with non-equilibrium chemistry and radiative cooling. We solve chemical networks of 54 reactions for 27 gas-phase species: H^+ , e^- , H , H^- , H_2 , D^+ , D , HD , C^+ , C , CH , CH_2 , CO^+ , CO , CO_2 , O^+ , O , OH^+ , OH , H_2O^+ , H_2O , H_3O^+ , O_2^+ , O_2 , Si , SiO , and SiO_2 . The chemical reaction rates are given in C15 for Si-bearing species, and in Omukai et al. (2010) for other species. We solve the chemical reactions implicitly to obtain the abundances of the gas-phase species in each fluid element at each time step. We then calculate the associated cooling and heating rates.

We implement radiative cooling by C^+ , C , and O , and by H_2 and HD molecules. We calculate the level populations for each species in a time-dependent manner. Gas opacity is explicitly calculated and the cooling rate for each emission line is reduced by a factor determined by the local velocity gradient in the optically thick regime (the so-called Sobolev approximation). We calculate the velocity gradient in the three directions x , y , and z as in Hirano & Yoshida (2013). We also include metal molecular line cooling, using the formulation and the cooling tables presented by Neufeld & Kaufman (1993) and Neufeld et al. (1995) for H_2O and Omukai et al. (2010) for CO and OH . We obtain the cooling rate $\Lambda_i(m)$ of molecules $m = \text{CO}$, OH , and H_2O with the parameter $\tilde{N}(m) = n(m)/|dv_i/dr_i|$ corresponding to optical depth under the large velocity gradient (LVG) approximation in the three directions $i = x, y$, and z , and take the average as $\Lambda(m) = [\Lambda_x(m) + \Lambda_y(m) + \Lambda_z(m)]/3$.

We calculate the optical depth for the continuum emission as $\tau_{\text{con}} = (\kappa_{\text{g}}\rho_{\text{g}} + \alpha_{\text{d}})\lambda_{\text{J}}$, where κ_{g} and ρ_{g} are the absorption cross-section of the primordial gas (Mayer & Duschl 2005) and mass density of the gas component, respectively. The absorption coefficient α_{d} for grains is calculated for all grain size and species as Equation (8) of C15. To save the computational cost, we use the one-zone model with the shielding length $\lambda_{\text{J}} = (\pi c_{\text{s}}^2/G\rho)^{1/2}$. The emission rate of each transition line is further reduced by a factor of $e^{-\tau_{\text{con}}}$. We consider the continuum emission by collision-induced emission (CIE) of hydrogen molecules (Yoshida et al. 2006) and by dust grains. These continuum emission rates are multiplied by escape fraction $\beta_{\text{con}} = \min\{1, \tau_{\text{con}}^{-2}\}$ (Omukai 2000).

Hydrogen molecules are formed via endothermic reactions with $E = 4.48$ eV per formed molecule. The three-body

reactions particularly enhance the temperature at densities $10^8\text{--}10^{11} \text{ cm}^{-3}$. Tsuribe & Omukai (2008) find that the gas heating resulting from the rapid hydrogen molecular formation mitigates the cloud deformation and makes the cloud core rounder. We consider the heating mechanism according to the formulation of Hollenbach & McKee (1979) and Omukai (2000).

2.2 Grain growth

The dust species considered here are metallic silicon (Si), metallic iron (Fe), forsterite (Mg_2SiO_4), enstatite (MgSiO_3), amorphous carbon (C), silica (SiO_2), magnesia (MgO), troilite (FeS), and alumina (Al_2O_3), which are major species condensed in unmixed SN ejecta (Nozawa et al. 2003, 2007). We follow the evolution of the size distributions and abundances of the grain species by essentially treating the grain growth as chemical reactions. We consider 13 reactions as in C15. We integrate the growth rate (Equation 9 in C15) to derive the grain radius and condensation efficiency at each time for each fluid element. We then calculate the reaction rate of hydrogen molecular formation on grain surfaces, radiative cooling efficiency, and continuum opacity for every grain species and radius.

2.3 Particle splitting

We need to follow the gas cloud collapse to very high densities. The Jeans length of the central, densest part decreases eventually down to ~ 0.1 AU when a protostellar core is formed. To save the computational cost, we use the particle splitting technique, when the resolution is about to violate the Jeans criterion (Truelove et al. 1997, 1998). Dense gas particles are replaced with less massive daughter particles. In Chiaki & Yoshida (2015), we present a novel method in which the daughter particles are distributed based on the Voronoi diagram tessellated by parent particles. With this method, the density structures of the cloud is well preserved. In the entire course of our simulations, a Jeans mass is required to be resolved by more than $1000M_{\text{min}}$, where $M_{\text{min}} = N_{\text{ngb}}m_{\text{p}}$ is the minimal resolvable mass of the parent SPH particles with mass m_{p} , and N_{ngb} is the number of the neighbor particles. We set $N_{\text{ngb}} = 64 \pm 8$, and thus the Jeans mass is always resolved by $\sim 10^5$ particles.

2.4 Later accretion phase

As the density in the central core increases, the dynamical time decreases and the necessary integration time step gets progressively shorter. Sink particle techniques are often employed to save computational time, where the gas inside a pre-determined accretion radius is replaced with a sink particle (Dopcke et al. 2013; Safronek-Shrader et al. 2014b; Smith et al. 2015). The evolution of a circumstellar disk, through which the gas is accreted, is not followed accurately with sink particle techniques. It is also known that the separation of fragments depends on the accretion radius (Machida & Doi 2013; Greif et al. 2012). Instead of employing a sink particle technique, we resort to following the gas dynamics in and around the proto-stellar core by setting the specific heat ratio to be $\gamma = 1.4$ after the density of

Table 1. Properties of gas clouds

Cloud	z_{form}	$M_{\text{vir}}^{\text{dm}}$	$M_{\text{vir}}^{\text{ba}}$	R_{vir}	M_{PopIII}	α	β	λ	$\varepsilon_{\text{turb}}$
UNI	—	0.0×10^0	2.2×10^6	551	—	0.51	0.0069	0.015	0.350
MH1	20.46	1.4×10^5	2.0×10^4	26.5	283.9	0.46	0.0049	0.011	0.086
MH2	16.20	1.4×10^5	3.7×10^4	46.8	751.3	0.48	0.0320	0.050	0.069
MH3	15.15	8.1×10^4	1.6×10^4	37.5	60.5	0.99	0.0325	0.063	0.067

Note — z_{form} is formation redshift of the minihalos. $M_{\text{vir}}^{\text{dm}}$ [M_{\odot}] and $M_{\text{vir}}^{\text{ba}}$ [M_{\odot}] are mass of the dark matter and baryon, respectively, within the Virial radius R_{vir} [pc] within which the average density is 200 times cosmological average. $\alpha = \bar{\varepsilon} R_{\text{vir}} / GM_{\text{vir}}$ and $\beta = 5E_{\text{rot}} R_{\text{vir}} / 3GM_{\text{vir}}^2$ are the ratios of thermal and rotational energy to gravitational energy, where $\bar{\varepsilon}$ is the mass-weighted average of specific energy over SPH particles within R_{vir} , E_{rot} is the sum of the rotational energy $m|\mathbf{r} \times \mathbf{v}|^2 / 2r^2$ of an SPH particle with mass m , coordinate \mathbf{r} , and velocity \mathbf{v} , and $M_{\text{vir}} = M_{\text{vir}}^{\text{dm}} + M_{\text{vir}}^{\text{ba}}$ is the total mass within radius R_{vir} . $\lambda = \bar{j} / \sqrt{2} V_{\text{vir}} R_{\text{vir}}$ is the spin parameter (Bullock et al. 2001), where \bar{j} is the mass-weighted average of specific angular momentum $j = |\mathbf{r} \times \mathbf{v}|$ and $V_{\text{vir}} = \sqrt{GM_{\text{vir}} / R_{\text{vir}}}$ is the circular velocity at the Virial radius. $\varepsilon_{\text{turb}} = \bar{v}_{\text{turb}}^2 / (\bar{v}^2 + \bar{c}_s^2)$ is the ratio of the turbulent energy to the internal energy, where \bar{v}_{turb} is the root-mean-square of velocity as used by Mac Low (1999), and \bar{v} and \bar{c}_s are the mass-weighted averages of kinetic and sound velocities, respectively. These values are measured when the peak density reaches $n_{\text{H,peak}} = 10^{-3} \text{ cm}^{-3}$ for metallicity $Z = 10^{-4} Z_{\odot}$.

Table 2. Properties of heavy elements and dust grains

(a) Abundance of heavy elements

X	C	O	Mg	Al	Si	S	Fe
A_X	1.08×10^{-4}	1.19×10^{-3}	4.19×10^{-5}	8.29×10^{-7}	6.67×10^{-5}	3.01×10^{-5}	6.76×10^{-6}
$[X/\text{Fe}]$	0.22	1.01	0.77	0.14	0.99	1.01	0.00

Note — Abundances of heavy elements released by a Pop III SN with progenitor mass $30 M_{\odot}$ in an ambient gas with density $n_{\text{amb}} = 1 \text{ cm}^{-3}$ (Nozawa et al. 2007). We show the number abundances relative to hydrogen nuclei with metallicity $Z = Z_{\odot}$. The values are reduced by the factor Z/Z_{\odot} for metallicity Z . In the second row, the relative abundance $[X/\text{Fe}] = \log(A_X/A_{\text{Fe}}) - \log(A_{X,\odot}/A_{\text{Fe},\odot})$ is shown. The solar abundance $A_{X,\odot}$ is taken from Caffau et al. (2011a).

(b) Composition and characteristic size of grain species

i	Silicon	Iron	Forsterite	Enstatite	Carbon	Silica	Magnesia	Troilite	Alumina	Total
$f_{\text{dep},i,0} [\times 10^{-3}]$	29.14	1.93	0.77	< 0.01	0.62	5.27	1.34	0.45	< 0.01	39.53
$r_{i,0}^{\text{grow}} [\times 10^{-2} \mu\text{m}]$	38.67	28.30	1.20	1.38	1.97	5.76	5.31	3.53	0.11	

Note — Initial depletion factor $f_{\text{dep},i,0}$ relative to total mass of metal and dust and the characteristic radius $r_{i,0}^{\text{grow}} = \langle r^3 \rangle_i / \langle r^2 \rangle_i$ of grain species i .

fluid elements exceeds $n_{\text{H}} = 10^{16} \text{ cm}^{-3}$, where the gas becomes optically thick even in a primordial gas. Although we are not able to follow the thermal evolution accurately beyond $n_{\text{H}} = 10^{16} \text{ cm}^{-3}$, the treatment allows us to examine gas fragmentation owing to dust thermal emission, which is expected to be effective at $n_{\text{H}} \gtrsim 10^{12} - 10^{15} \text{ cm}^{-3}$.

2.5 Initial conditions

2.5.1 Cloud models

We use two different sets of initial conditions; one spherical cloud as a controlled simulation, and three clouds hosted by small dark matter halos selected from cosmological simulations.

Uniform density cloud

The spherical cloud has a uniform density $n_{\text{H,ini}} = 0.1 \text{ cm}^{-3}$ and temperature $T_{\text{ini}} = 300 \text{ K}$. The cloud radius and mass are $R_{\text{ini}} = 551 \text{ pc}$ and $M_{\text{ini}} = 2.3 \times 10^6 M_{\odot}$, corresponding to the half Jeans length and the

Jeans mass, respectively, for the uniform cloud with density $n_{\text{H,ini}}/f_{\text{enh}}$, where $f_{\text{enh}} = 1.8$ is the enhancement factor (Matsumoto & Hanawa 2003). We first put SPH particles in a box with length $2R_{\text{ini}}$ on a side with a random seed. Since the amplitude of density perturbation resulting from Poisson noise is too large, we perform the preliminary calculation without gravity to relax the perturbation. The calculation is performed with the isothermal equation of state in a periodic boundary box until the root-mean-square of particle density becomes 0.1 of the mean density (the same level as the simulations of Machida & Nakamura 2015). Then we cut out the gas sphere with radius R_{ini} .

We impose solid rotation such that the rotation energy relative to the gravitational energy $\beta_{\text{ini}} = \Omega_{\text{ini}}^2 R_{\text{ini}}^3 / 3GM_{\text{ini}}$ is 10^{-3} , corresponding to the angular velocity $\Omega_{\text{ini}} = 1.4 \times 10^{-17} \text{ s}^{-1}$. The initial number fractions of deuterium and helium relative to hydrogen nuclei are 5.3×10^{-5} and 0.079, respectively. The number fractions of electron and hydrogen molecules relative to hydrogen nuclei are $y(e) = 10^{-4}$ and $y(\text{H}_2) = 10^{-6}$, respectively. Both deuterium and helium are initially assumed to be in neutral atoms. The spherical

cloud calculations are dubbed “UNI” hereafter. The cosmic microwave background (CMB) radiation contribute to the gas heating by exciting the level populations and giving the energy with grains. For UNI, we assume the CMB temperature $T_{\text{CMB}} = 45$ K, corresponding to the redshift $z \simeq 15$.

Minihalos

We also perform collapse simulations for gas clouds hosted by minihalos chosen from the cosmological simulations of Hirano et al. (2014) (hereafter H14). From the large simulation box of ~ 1 Mpc on a side, we cut out the spherical region including dark matter particles centered at a minihalo with radii ~ 1 kpc so that sound waves cannot cross the region during the cloud collapse. The abundances of primordial species are inherited from the cosmological simulations. The CMB temperature is calculated from $T_{\text{CMB}} = 2.73(1 + z_{\text{form}})$ K at formation redshift z_{form} of the halos.

We select three minihalos dubbed “MH1”, “MH2”, and “MH3”, which cover the different types of the early clouds. Their properties are presented in Table 1. The sixth column shows the final stellar mass M_{PopIII} derived by the collapse simulations without metal performed by H14. For MH1, MH2, and MH3, $M_{\text{PopIII}} = 283.9, 751.3,$ and $60.5 M_{\odot}$, respectively. The difference of stellar mass is affected by the different thermal evolution from clouds to clouds as discussed in Appendix C of H14 and below.

Cloud properties

Various parameters can characterize gas clouds. In Table 1, we show the mass of baryon $M_{\text{vir}}^{\text{ba}}$ and dark matter $M_{\text{vir}}^{\text{dm}}$ within the Virial radius R_{vir} within which the average density is 200 times larger than the cosmological average density and the over-dense region turns to collapse against the cosmic expansion (Peebles 1980). These parameters characterize the depth of potential well $GM_{\text{vir}}/R_{\text{vir}}$ created by the halos, where $M_{\text{vir}} = M_{\text{vir}}^{\text{ba}} + M_{\text{vir}}^{\text{dm}}$. The collapse timescale of cloud is expected to become longer with shallower potential. As H14 predict, the collapse time will affect the thermal evolution of clouds.

The ratios α and β of thermal and rotational energy to the gravitational energy could also have effects on cloud fragmentation as discussed by Tsuribe & Inutsuka (1999a,b). For UNI, MH1, and MH2, $\alpha \simeq 0.5$ and small β ($\beta < 0.1$), which predicts that the clouds are marginally unstable. For MH3, large α ($\simeq 1$) would lead the cloud to collapse monolithically. However, we should note that the prediction is based on the semi-analytical model where gas evolves isothermally (see Figure 8 in Tsuribe & Inutsuka 1999b). The low-metal clouds no longer evolve isothermally. Another parameter which characterizes the spin is λ , which is defined as the ratio between angular momentum of clouds and that of gravitationally bound object. Jappsen et al. (2007) find that the parameter have little effects on the cloud evolution in the earlier stage of collapse ($n_{\text{H, cen}} < 500 \text{ cm}^{-3}$) when $\lambda \lesssim 0.05$. We aim to see how the cloud rotation has effect on the later stage of collapse.

In Table 1, we also present the parameter of turbulent motion $\varepsilon_{\text{turb}}$ as the ratio of turbulent energy to the internal energy. For minihalos (MH1, MH2, and MH3), the clouds are less turbulent ($\varepsilon_{\text{turb}} = 0.067\text{--}0.086$) while the random den-

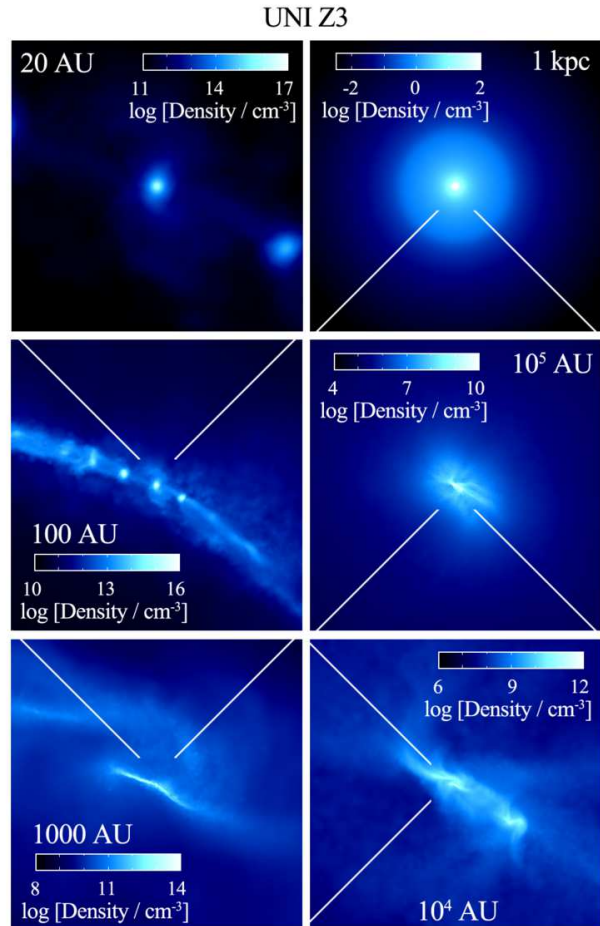


Figure 1. Zoom-in distribution of the density-weighted density projection centered at the most dense region of the cloud UNI Z3 at 36.4 years after the first protostar formation. The side length of the panels becomes shorter clockwise from top-right (1 kpc) to top-left (20 AU). This cloud fragments into two clumps owing to the OH molecular cooling at the length scale ~ 1000 AU (bottom-right panel). The inner part of the left clump further fragments into three protostellar cores and several diffuse blobs by dust thermal emission at the length scale ~ 10 AU (middle-left).

sity perturbation is converted to the large turbulent motion for UNI when the peak density is 10^3 cm^{-3} ($\varepsilon_{\text{turb}} = 0.350$). The turbulence might affect the fragmentation properties of the clouds (Dopcke et al. 2013; Smith et al. 2015).

2.5.2 Metal and dust properties

In our simulations, metals and dust are uniformly added to the simulation gas particles. The metal abundance, dust condensation efficiency, and dust size distribution are taken from a model of nucleosynthesis and grain formation/destruction in a Pop III SN. For the first time, we adopt such the realistic initial conditions to the three-dimensional simulations of the Pop II star formation, while previous works often assume the solar abundance pattern. We employ a Pop III SN model taken from Nozawa et al. (2007). We here make use of the model with the progenitor mass

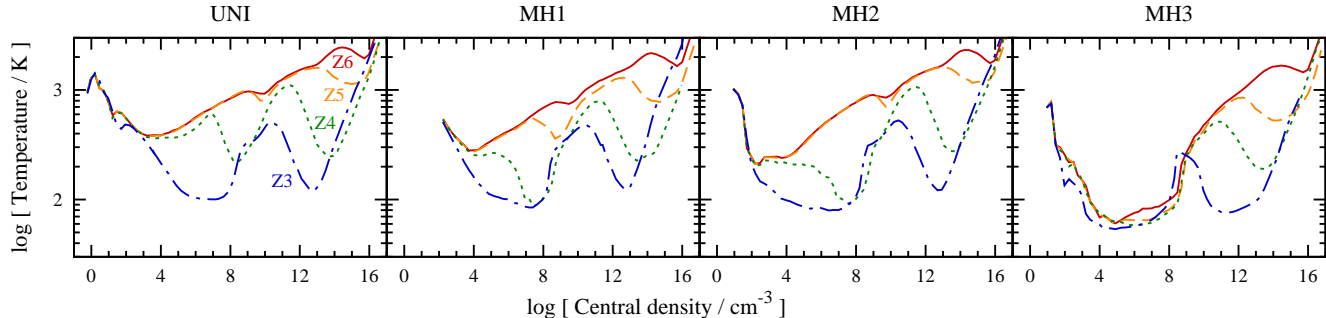


Figure 2. Thermal evolution of the cloud cores with metallicities 10^{-6} (Z6; red solid), 10^{-5} (Z5; orange dashed), 10^{-4} (Z4; green dotted), and $10^{-3} Z_{\odot}$ (Z3; blue dot-dashed) for clouds UNI, MH1, MH2, and MH3 from left to right.

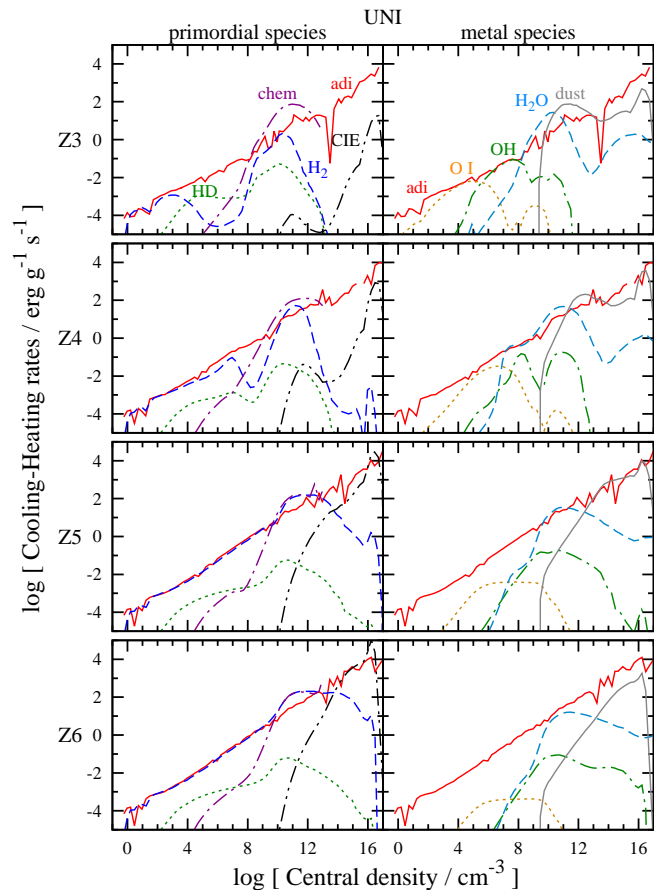


Figure 3. Thermal evolution of cooling/heating rates for Z6, Z5, Z4, and Z3 from top to bottom for cloud UNI. Left and right panels show the cooling efficiencies of the primordial and metal species, respectively. “adi” depicts the adiabatic compressional heating rate, and “chem” depicts the absolute value of net heating/cooling efficiency owing to H_2 formation/dissociation.

$30 M_{\odot}$ and the ambient gas density $n_{\text{amb}} = 1 \text{ cm}^{-3}$ as a characteristic model.

The progenitor mass determines the abundance of heavy elements. The mass spectrum of Pop III star has the bimodal distribution as predicted by H14 and Hirano et al.

(2015). In their simulations, the first peak lies around $30 M_{\odot}$. Susa et al. (2014) also predict the peaky distribution with characteristic mass $20\text{--}30 M_{\odot}$. In our simulation, employed M_{pr} is limited to $30 M_{\odot}$. We discuss the fragmentation property for clouds enriched by progenitors with various masses in Section 5.

The dust grains are formed in expanding SN ejecta, and destroyed by the reverse shocks. The strength of the destruction depends on the ambient gas density n_{amb} . Just before the explosion, n_{amb} is determined by the interaction between gas and ultraviolet photons emitted from a main-sequence (MS) Pop III star. The H II region generally has the nearly uniform density by the strong radiation pressure with $n_{\text{amb}} = 0.1\text{--}1 \text{ cm}^{-3}$ (Kitayama et al. 2004; Whalen et al. 2004). Here, we conservatively set the ambient gas density as 1 cm^{-3} .

We briefly summarize the difference between the Pop III SN model and the present-day model. First, the number fractions of the light elements relative to iron are larger in the latter case (second row of Table 2a). In particular, the Pop III model predicts a large fraction of $[O/Fe] \simeq 1$. We thus expect that the radiative cooling by OH and H_2O molecules is more efficient than in the case of solar abundance. Second, the total condensation efficiency of metal is only 4%, which is much smaller than $\sim 50\%$ in the present-day. Although the grain growth can enhance the final dust-to-gas mass ratio, the efficiency of H_2 formation on grains and dust cooling rate are still smaller than in the present-day case.

The Pop III SN model gives us the relative abundances of metal and dust. Their absolute values are determined for a given metallicity, or the total mass fraction of heavy element to the gas. We examine four cases with metallicities 10^{-6} , 10^{-5} , 10^{-4} , and 10^{-3} times the solar value $Z_{\odot} = 0.02$. Hereafter we call the models as Z6, Z5, Z4, and Z3, respectively. We assume that initially all of C nuclei are in the form of C^+ , and O and Si are in neutral atoms. The initial mass fraction $f_{\text{dep},i,0}$ of grain species i relative to metal and the characteristic radius of grains (see C15) are shown in Table 2 (b).

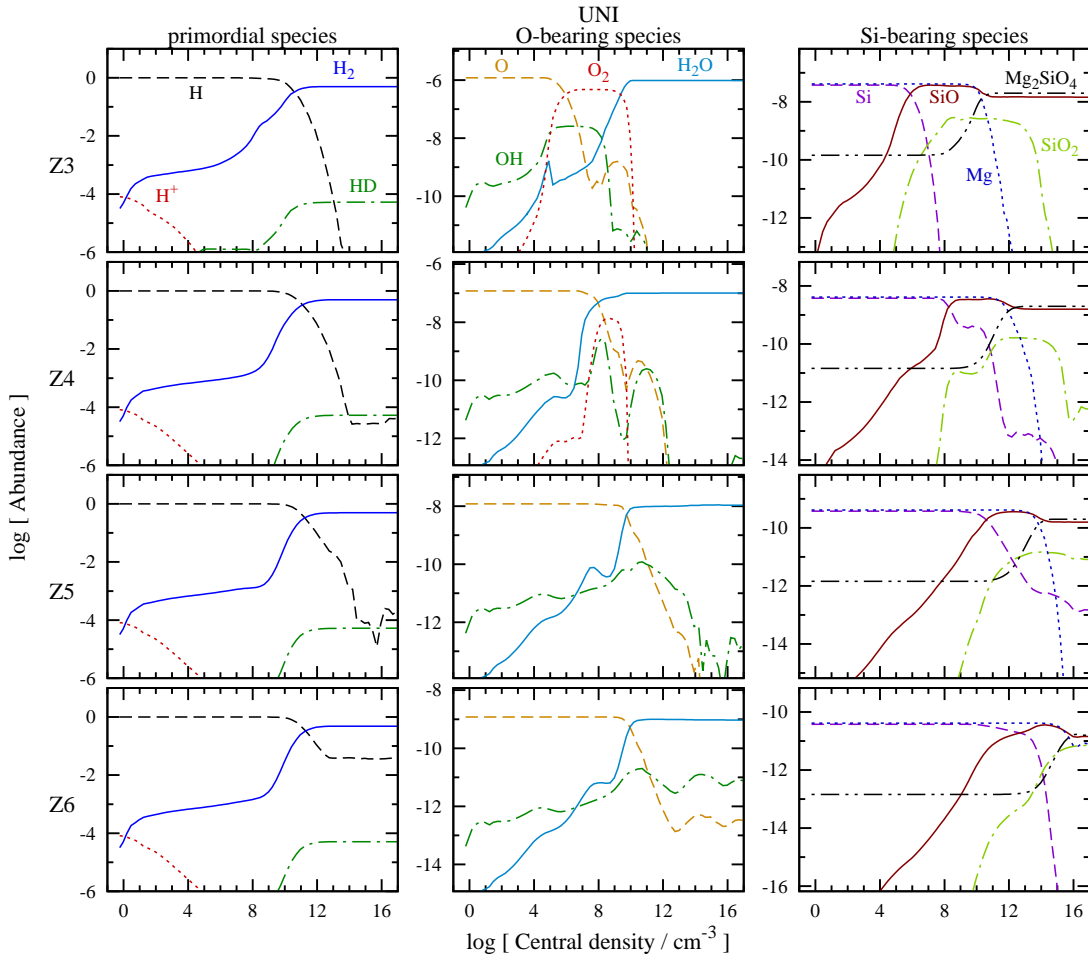


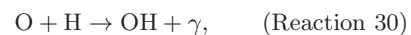
Figure 4. Chemical abundance of primordial species (left column), O-bearing species (middle), and Si-bearing species (right) for Z6, Z5, Z4, and Z3 from top to bottom for UNI.

3 CHEMO-THERMAL EVOLUTION OF SPHERICAL CLOUDS

Figure 1 shows the zoom-in image of our simulated cloud UNI Z3. Particle splitting allows us to follow the nonlinear gravitational evolution from a diffuse interstellar cloud to protostellar core(s) over 20 orders of magnitude in density. The mass resolution M_{\min} is initially $320 M_{\odot}$ and eventually reaches $3.2 \times 10^{-5} M_{\odot}$ (10 Earth masses), corresponding to $\lesssim 0.06$ AU, in the central densest region with $\gtrsim 10^{16} \text{ cm}^{-3}$ after splitting particles seven times. We in this section see the temperature evolution, comparing to the cooling/heating efficiencies for UNI cloud. Figure 2 shows the temperature evolution as a function of the central density with metallicities 10^{-6} – $10^{-3} Z_{\odot}$ of clouds UNI, MH1, MH2, and MH3.¹ Figures 3 and 4 show the cooling/heating efficiencies and the abundances of gas- and solid-

phase species as a function of the central density for UNI Z3–6.

Adiabatic compressional heating is dominant for all the metallicity cases at densities $\lesssim 1 \text{ cm}^{-3}$. After that, molecular hydrogen cooling becomes important until the density reaches the critical value for H₂ molecules, $n_{\text{H}} \sim 10^3 \text{ cm}^{-3}$, where the level populations thermalize and approach their LTE values. For Z4–6, the temperature increases only slowly by the balance between the gas compressional heating and H₂ line cooling. For Z3, the fine-structure line cooling by O I becomes efficient. Thereafter, OH molecules form via the reaction



and then OH cooling becomes dominant at $n_{\text{H}} \sim 10^4$ – 10^8 cm^{-3} for Z3. The gas fragments into two clumps by efficient OH cooling for Z3 as shown in Figure 1.

At the same time, hydrogen molecules are formed on grain surfaces. The binding energy is released and converted into the gas thermal energy. Although the heating rate of grain-surface reaction dominates over that of the other reactions, it never exceeds the cooling efficiency by rotational transition line cooling of OH molecules. Only by the grain-surface reaction, cloud cores do not become fully molecular

¹ Hereafter, we measure the quantities such as the temperature, density, chemical abundance, and cooling rate in the central region by mass-weighting over the gas particles with densities $n_{\text{H}} > n_{\text{H,peak}}/3$, where $n_{\text{H,peak}}$ is the largest density in each snapshot.

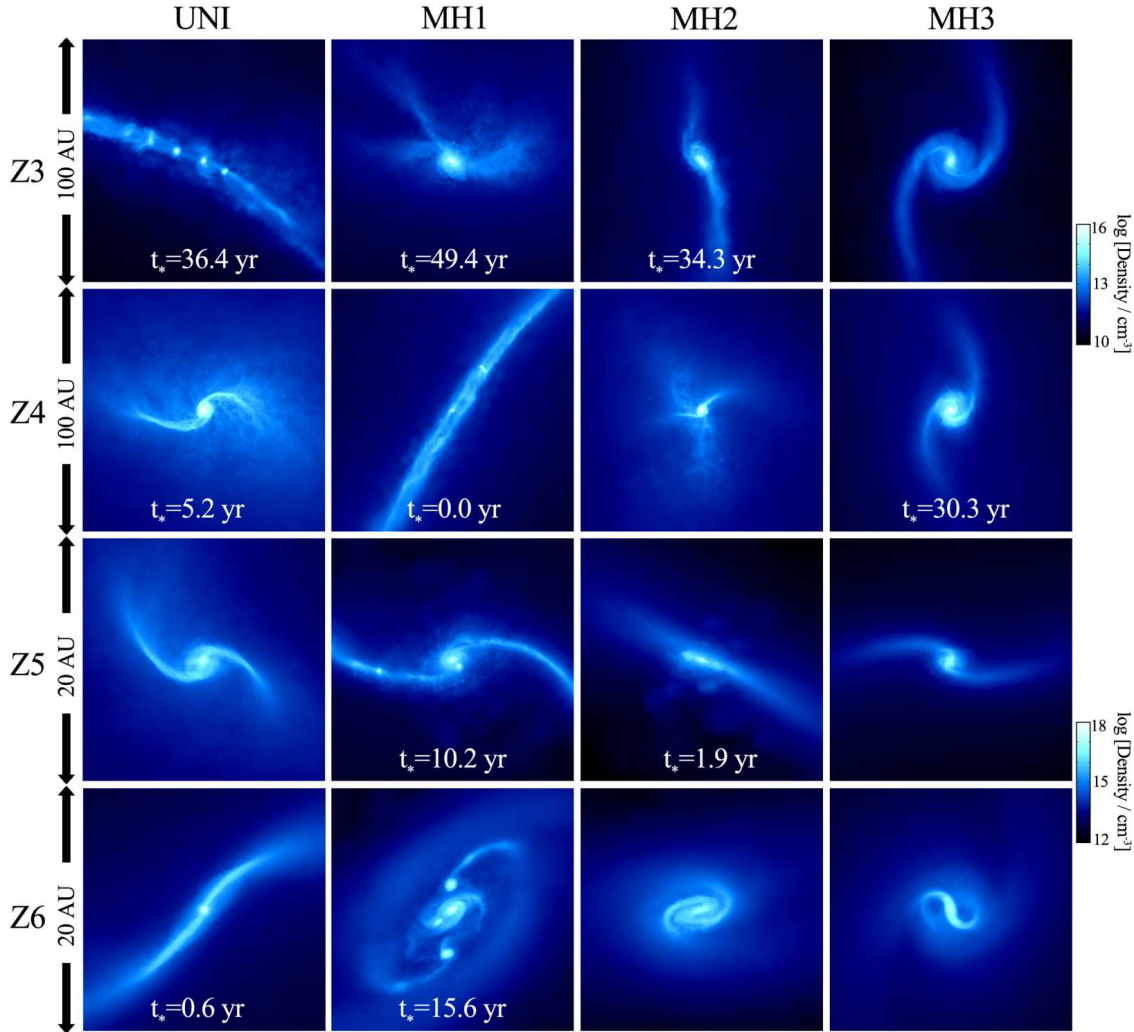
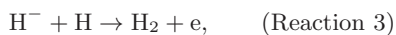
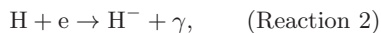
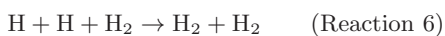
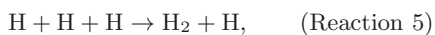


Figure 5. Density-weighted density projection of the clouds UNI, MH1, MH2, and MH3 from left to right with metallicities 10^{-6} , 10^{-5} , 10^{-4} , and $10^{-3} Z_{\odot}$ from bottom to top at the time where the simulations are terminated. The plotted region is 100 AU (upper 8 panels) and 20 AU (lower 8 panels) on a side. The color contour depicts the density $n_{\text{H}} = 10^{10}\text{--}10^{16} \text{ cm}^{-3}$ (upper 8 panels) or $10^{12}\text{--}10^{18} \text{ cm}^{-3}$ (lower 8 panels) from black to white. These snapshots are output at the time t_* from the first protostar is formed as written in the bottom of each pane. In the models without the time, the central blob does not satisfy our criterion of a protostar (see footnote 2) until the end of the simulation.

until the density reaches $\sim 10^8 \text{ cm}^{-3}$. The molecular fraction reaches 3×10^{-3} . For Z4–6, the molecules are formed only via H^- processes as



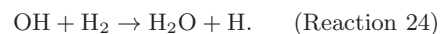
and molecular fraction becomes 2×10^{-4} . At density $\sim 10^8 \text{ cm}^{-3}$, the three-body H_2 formation reactions



operate, and the clouds get fully molecular. At this moment, the exothermic reactions raise the gas temperature rapidly. Then the specific heat ratio temporarily exceeds the critical value of 4/3 for gravitational collapse. Then a pressure-

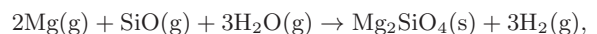
supported core surrounded by accretion shock is formed for Z3. The velocity jump is seen at the rapid heating works.

The gas temperature continues to increase to $\sim 10^{11} \text{ cm}^{-3}$ while the H_2O molecules act as a main coolant. The H_2O molecules are formed via the reactions



For Z5, H_2O cooling is a dominant cooling process in a narrow range of density around 10^{10} cm^{-3} as shown by the cyan curve in Figure 3.

Dust cooling becomes efficient at $10^{11}\text{--}10^{13} \text{ cm}^{-3}$ for Z3, and at slightly larger densities $10^{12}\text{--}10^{14} \text{ cm}^{-3}$ for Z4. The grain growth enhances the efficiency of the dust thermal emission for Z3–5. Forsterite grains grow rapidly via the reaction



where (g) and (s) denote the species in the gas- and solid-

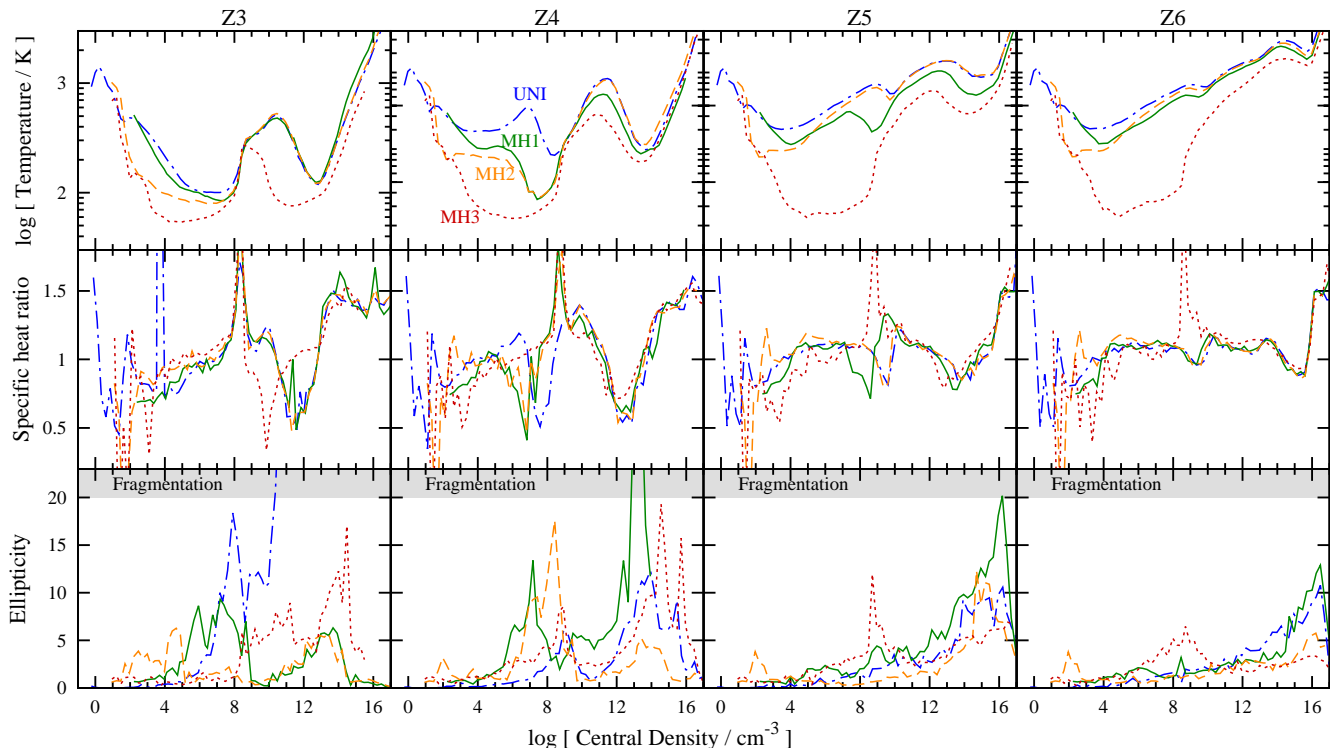


Figure 6. Temporal evolution of the temperature (top), specific heat ratio (middle) and ellipticity \mathcal{E} (bottom) as a function of the central density of cloud cores UNI (blue dot-dashed), MH1 (green solid), MH2 (orange dashed), and MH3 (red dotted) for Z3–6 from left to right. We measure the specific heat ratio as $\gamma = (\Delta T/T)/(\Delta\rho/\rho) + 1$, where Δx is the difference of the quantity x between a snapshot and its previous snapshot. We arrange the output times such that the maximum density $n_{\text{H,peak}}$ increases 0.25 dex between the two adjacent outputs. The grey shaded region in the bottom panels indicates the ellipticities $\mathcal{E} > 20$ (see text) for which the cloud breaks up into multiple clumps.

phases, respectively. The magnesium atoms are eventually exhausted (see blue dotted curve in Figure 4). For Z6, although there is little amount of dust, the temperature drops at 10^{14} cm^{-3} by collision-induced continuum cooling (black dot-dot-dashed curve in Figure 3).

Dust cooling becomes ineffective when thermal coupling between the gas and grains is established. The cloud core becomes optically thick soon after this phase, at densities 1×10^{13} , 3×10^{14} , 3×10^{15} , and $1 \times 10^{16} \text{ cm}^{-3}$ for Z3, Z4, Z5, and Z6, respectively. The gas pressure rapidly increases in the region where radiative cooling is inefficient due to the large opacity, and then a hydrostatic core bounded by accretion shock is formed. The second velocity jump appears in the velocity profile as well as at the density where H_2 formation heating proceeds. Just inside the shock, the gas disk is formed, being supported by the rotation. As the temperature further increases toward the center, the central part becomes spherical because of the strong pressure support. Here, let us define a pressure-supported “protostar” as the region bounded by a sufficiently spherical iso-density surface.² The cloud fragmentation again occurs for Z3 around

the time of the first protostar formation as shown in Figure 1.

4 CLOUD FRAGMENTATION

4.1 Thermal evolution and fragmentation of cloud

4.1.1 Overview of the global feature

In order to see whether the gas clouds fragment or not, we follow the evolution over several tens years after the first protostar appears. Figure 5 shows the snapshots output at the time t_* after the first protostar formation. Contrary to the popular notion that cloud fragmentation conditions are largely determined by the gas metallicity, the fragmentation properties are different even with the same metallicity (see panels in each row for a given metallicity). For example, for MH3 Z4, fragmentation does not occur even 30 years after the first protostar formation, while multiple clumps are already formed before the first protostar is formed for

with the major- and minor-axes a and b , we obtain the ellipticity $\mathcal{E} = a/b - 1$ of each iso-density surface. We then define the protostellar surface as the least dense (most distant from the center) surface that satisfies $\mathcal{E} < \mathcal{E}_*$ with the critical ellipticity $\mathcal{E}_* = 0.3$. The protostellar mass is only 20% smaller with a smaller threshold of $\mathcal{E}_* = 0.2$.

² In practice, we calculate iso-density contours by dividing the gas into 100 density bins equally separated with a logarithmic scale from $\log(n_{\text{H,peak}}) - 3$ to $\log(n_{\text{H,peak}})$. Fitting the distribution of the gas particles in each density bin by an ellipsoid

MH2 Z4. Clearly, whether a cloud fragments or not is not determined solely by the gas metallicity.

In other words, the thermal evolution, which critically affects the fragmentation property, is not uniquely determined by the gas metallicity. The top panels of Figure 6 shows the temperature evolutions as a function of the central density of four clouds for Z5 and Z4. The evolutionary tracks on the $n_{\text{H}}-T$ plane vary significantly even with a fixed metallicity. The variation would generate the different fragmentation property as discussed in more detail later. We begin with discussing the physical processes that drive the variation of the thermal evolution in Section 4.2. Then we discuss the effect of the thermal evolution on the cloud fragmentation in Section 4.3. Finally, in Section 4.4, we derive criteria for cloud fragmentation.

4.1.2 Filament fragmentation vs. disk fragmentation

We note an important point that the cloud fragmentation is observed also at a very small metallicity of $10^{-6} Z_{\odot}$, where dust cooling is not efficient. For MH1 Z6, the perturbations grow in the spiral arms in a circumstellar disk with a size of $\simeq 10$ AU around the central most massive core. Such a structure is reported also by Clark et al. (2011) and Greif et al. (2012) in the case without metal or dust. Whereas, the simulations with intermediate metallicities $10^{-5}-10^{-3} Z_{\odot}$ show a different type of fragmentation. For UNI Z3, MH1 Z4, and MH1 Z5, the ‘‘peapod’’-like structure, where several protostellar cores are hosted in a long filament extending over $\sim 20-100$ AU, appears. Such a peculiar structure is formed typically when dust cooling operates, as we discuss later.

Hereafter, we distinguish the former and latter types of fragmentation as *disk fragmentation* and *filament fragmentation*, respectively. Since the disk fragmentation has been discussed in previous numerical studies (Clark et al. 2011; Greif et al. 2012), we in this paper focus on the filament fragmentation, and revisit the disk fragmentation briefly in Section 4.5.

4.2 Collapse timescale and the thermal evolution

As described in Section 4.1.1, the thermal evolution has an effect on the cloud fragmentation property even with a fixed metallicity. We find that the different thermal evolution among clouds can be explained by the variation of the collapse timescale. In a slowly collapsing cloud, the adiabatic compressional heating rate per unit volume

$$\Gamma_{\text{adi}} = -\rho p \frac{d}{dt} \left(\frac{1}{\rho} \right) = \frac{p}{t_{\text{col}}} \quad (1)$$

is correspondingly small. Here, t_{col} is the collapse timescale written as

$$t_{\text{col}} = \frac{\rho}{d\rho/dt}. \quad (2)$$

Therefore, the evolutionary track on the $n_{\text{H}}-T$ plane tends to be located in a low-temperature region.

We measure in our simulations that the time interval over which the peak density increases from $n_{\text{H,peak}} = 10^2 \text{ cm}^{-3}$ to 10^{16} cm^{-3} is 3, 4, 11, and 19 Myr for UNI, MH1, MH2, and MH3 Z4, respectively. The cloud UNI contracts most rapidly while the cloud MH3 contracts most

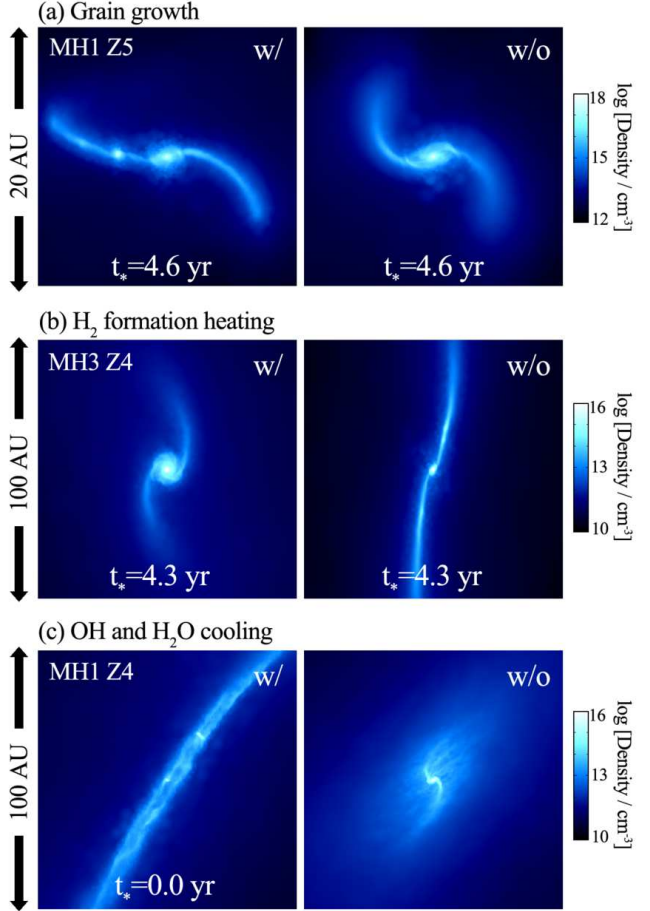


Figure 7. We compare the cloud fragmentation in the regular simulations (left) and controlled simulations (right) at the same epoch. All the relevant chemo-thermal processes are considered in the former simulations, while, in the latter simulations, (a) grain growth, (b) H_2 formation heating, and (c) OH and H_2O cooling are not included.

slowly among the four clouds. The evolutionary tracks in Figure 6 roughly trace the trend; the temperature of UNI remains high at all densities because of its slow rotation and hence the most rapid collapse. Contrastingly, the temperature of MH3 remains low because the large centrifugal force and the flat distribution of the dark matter slow the gas infall. We will discuss the origin of the different collapsing time in Section 5.

4.3 Important thermal processes

Figure 6 shows that different cooling and heating processes become important and characterize the various evolutionary tracks. For example, MH1 and MH3 Z5 enter the regime where dust cooling is efficient at $n_{\text{H}} \sim 10^{12}-10^{14} \text{ cm}^{-3}$ while UNI and MH2 do not. In addition to dust cooling, two other cooling and heating processes responsible to the fragmentation can be identified: H_2 formation heating and OH and H_2O cooling. We discuss the processes one-by-one in the following.

4.3.1 Dust cooling

Dust cooling is a crucial process to lower the gas temperature, to promote cloud elongation, and to induce the formation of low-mass fragments at high densities 10^{12} – 10^{15} cm^{-3} , where the Jeans mass is small $\sim 0.1 M_{\odot}$. Figure 6 clearly shows the effect of dust cooling on the filament formation for UNI Z3 and MH1 Z4 and Z5. The bottom panels present the cloud ellipticity $\mathcal{E} = a/b - 1$, where a and b are the major- and minor-axes of the cloud. The gas becomes unstable owing to the dust cooling at densities $n_{\text{H}} \sim 10^{12}$ – 10^{14} cm^{-3} , and bar-mode perturbations grow. A filamentary structure is formed as clearly seen in Figure 5. When the ellipticity becomes above 20–30, which is consistent with the critical value defined by Tsuribe & Omukai (2006), the dense filament quickly fragments to yield several protostars.

For UNI and MH2 Z5, even though the temperature decreases slightly by dust cooling at $n_{\text{H}} \sim 10^{12}$ – 10^{14} cm^{-3} , it is insufficient to enhance the ellipticity. The cloud ellipticity increases to only at most 11 and 12 for UNI and MH2, respectively. Figure 5 shows that short filaments are formed in these clouds, but without fragmenting to multiple clumps.

We emphasize that the growth of dust grains further enhances the cooling rate and thus promotes the gas elongation and fragmentation. In the Pop III SN dust model adopted here, Mg_2SiO_4 grains grow until gas-phase Mg atoms are exhausted at $\sim 10^{14}$ cm^{-3} . Figure 7 (a) compares our simulations with (left) and without (right) grain growth for MH1 Z5 at the same time $t_* = 4.6$ yr after the first protostar formation. While several protostellar cores are born from a filament in the case with grain growth, only a single protostar is formed at the center of a slightly more diffuse filament otherwise.

4.3.2 H_2 formation heating

In many cases, dust cooling becomes efficient at high densities but the gas cloud does not fragment. We find that chemical heating effectively makes the cloud stable against deformation. For example, in MH3 Z5, the rapid gas heating by the formation of H_2 molecules via three-body reactions becomes efficient at $n_{\text{H}} \sim 10^9$ – 10^{12} cm^{-3} . The temperature rapidly increases from 130 K at $n_{\text{H}} = 5 \times 10^8$ cm^{-3} to 700 K at 2×10^{11} cm^{-3} , causing the specific heat ratio to be 1.7 on average, which is sufficient to stabilize the gas against elongation. Then the gas ellipticity rapidly decreases from 12 to 2 as shown in the bottom panel of Figure 6.

The timescale for which the ellipticity increase from such a small value to the critical ellipticity is longer than the dynamical timescale of the cloud. In the clouds UNI, MH1, and MH2 with metallicities 10^{-4} – $10^{-3} Z_{\odot}$ and in the cloud MH3 with 10^{-6} – $10^{-3} Z_{\odot}$, the H_2 formation heating significantly suppresses the gas elongation before dust cooling becomes effective to promote the gas elongation.

Tsuribe & Omukai (2008) show that a gas cloud does not fragment with the metallicity range of 10^{-5} – $10^{-4} Z_{\odot}$, by an order of magnitude smaller than in our simulations. In their present-day dust model predicts 30 times larger efficiency of the H_2 molecular formation on grains than in our Pop III SN dust model (see Table 2 b). Hydrogen atoms are exhausted by the formation process before the molecular formation via three-body reactions at $n_{\text{H}} \sim 10^8$ cm^{-3} .

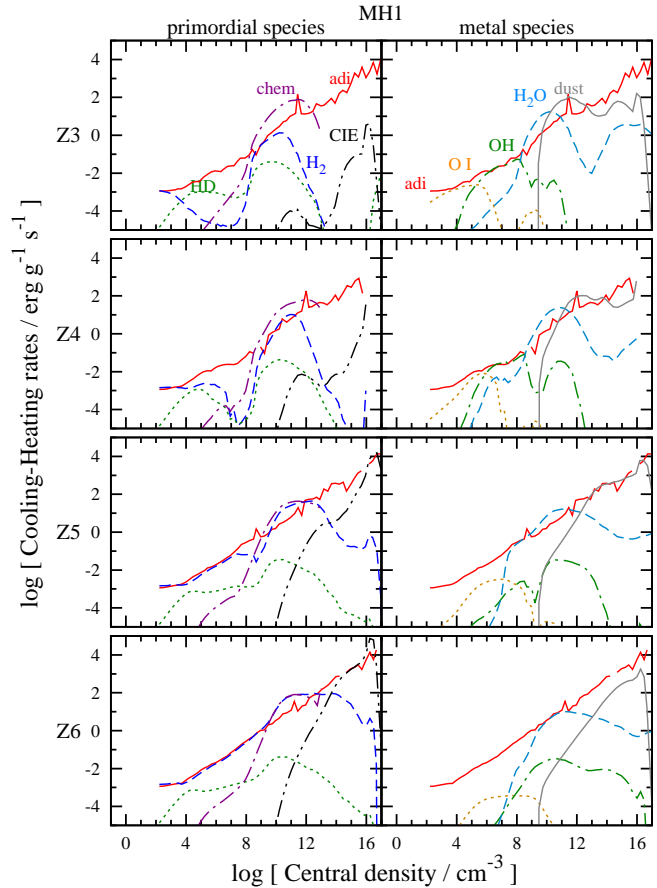


Figure 8. Same as Figure 3 but for cloud MH1.

In their model, H_2 formation heating therefore does not become efficient and can not stabilize the gas. Meanwhile, in our simulations even with 10^{-4} – $10^{-3} Z_{\odot}$, three-body reactions and the associated gas heating make the cloud rounder.

In order to see the effect more clearly, we perform a controlled simulation without the heating process. Figure 7 (b) shows the density distributions in the central 100 AU region of the cloud MH3 Z4 with (left) and without (right) H_2 formation heating. In the former case, the cloud core ellipticity \mathcal{E} remains around 3 because of the effective chemical heating at $\sim 10^8$ cm^{-3} . In the latter case \mathcal{E} increases up to 15 by OH cooling and then further increases to ~ 30 by dust cooling without any stabilization. Density perturbations in the filament grow and yield several protostellar cores in a thin filament.

4.3.3 OH and H_2O cooling

In the cloud MH1 Z4, although H_2 formation heating is effective (see the green solid curve in Figure 6), a thin filament is formed and quickly fragments to a few clumps. We find that radiative cooling owing to the transition lines of OH and H_2O molecules is important in this case. Figures 8 and 9 show the contribution of various heating and cooling processes as a function of density for the cloud. At $n_{\text{H}} = 10^6$ – 10^8 cm^{-3} , a large fraction of O atoms are converted into OH molecules (green dot-dashed curve), and OH cooling ex-

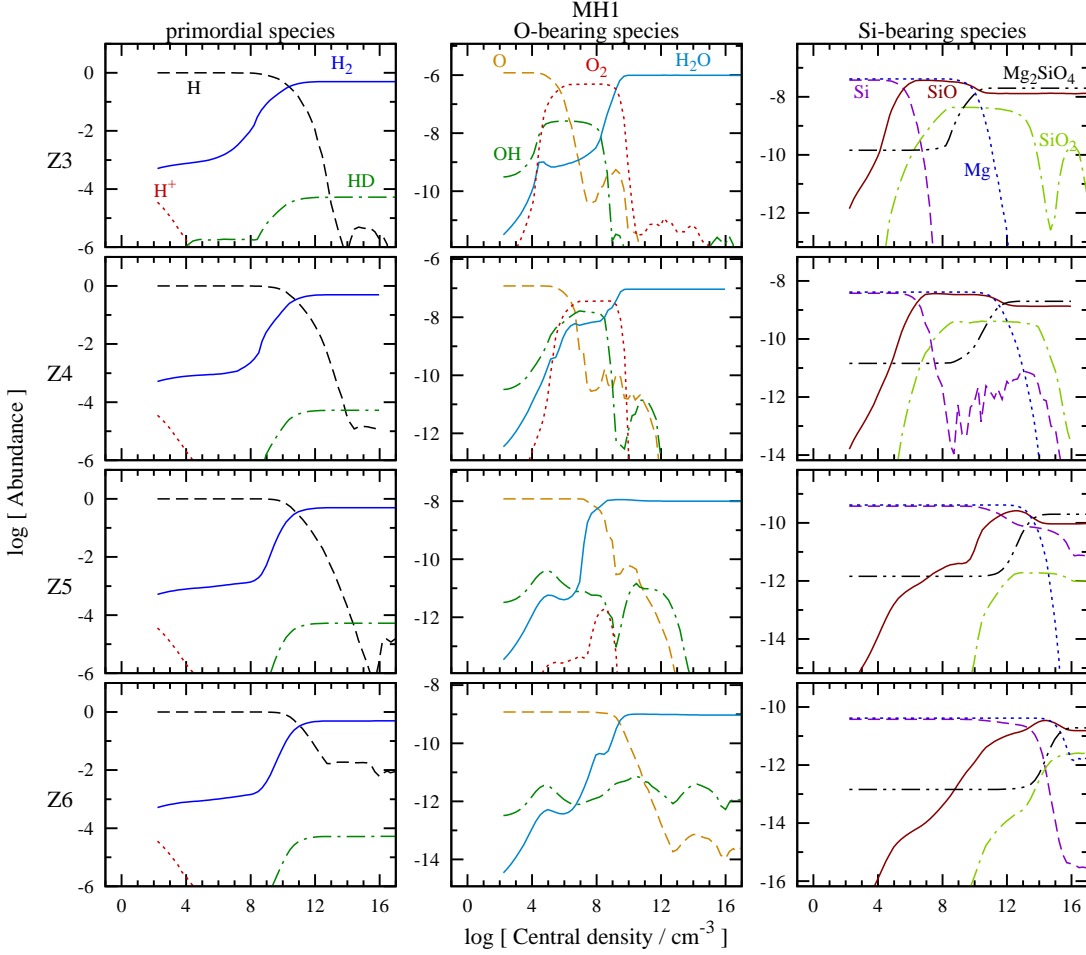


Figure 9. Same as Figure 4 but for cloud MH1.

ceeds the adiabatic compressional heating rate (red solid). Even though H_2 formation heating is effective at $n_{\text{H}} \sim 10^9\text{--}10^{11} \text{ cm}^{-3}$ and reduces the cloud ellipticity, \mathcal{E} evaluated at 10^{11} cm^{-3} is the largest among the four clouds for Z4 thanks to efficient OH and H_2O cooling. The cloud is then sufficiently elongated to trigger fragmentation. The ellipticity increases up to 33 in the end (see Figure 6). Although H_2O cooling is indeed effective for MH2 Z4 at $10^6\text{--}10^8 \text{ cm}^{-3}$ (orange dashed curve in Figure 6), it is not sufficient to compensate the stabilization effect by H_2 formation.

Again, in order to see clearly the effect of the OH and H_2O cooling, we perform a controlled simulation without OH and H_2O cooling for MH1 Z4. The result is shown in Figure 7 (c). Without the molecular cooling, even at densities where dust cooling is efficient, a single protostar is formed. Clearly, the efficient OH and H_2O cooling drives the formation of a long filament and subsequent fragmentation. This is for the first time demonstrated by our simulations which explicitly include the metal molecular cooling and the Pop III SN model with the large oxygen excess.

4.4 Criteria for first low-mass star formation

From the discussion in Sections 4.2–4.3, we can consider that the three thermal processes, dust cooling, H_2 formation

heating, and OH and H_2O cooling are important to determine the fragmentation properties of the clouds. Therefore, the criteria for gas fragmentation can be translated into the condition where these processes become effective or not for a given combination of the metallicity Z and the collapse timescale t_{col} . We define the fragmentation condition as

- (i) dust cooling is efficient at high densities $\sim 10^{12} \text{ cm}^{-3}$ to induce eventual elongation and fragmentation of clouds, and
- (ii-a) H_2 formation heating is not efficient at intermediate density $\sim 10^9\text{--}10^{11} \text{ cm}^{-3}$, or
- (ii-b) OH or H_2O cooling is efficient to trigger cloud elongation at density $\sim 10^6\text{--}10^8 \text{ cm}^{-3}$ even though H_2 formation heating later stabilizes the gas.

There remains a complexity that the collapse timescale itself varies when the cloud collapse proceeds faster/slower owing to gas cooling/heating. We thus introduce a parameter f_0 as an indicator of the collapse timescale that characterizes each cloud. The parameter satisfies the equation as

$$t_{\text{col}} = f_0 t_{\text{col}}^{\text{s}}(\gamma). \quad (3)$$

The factor $t_{\text{col}}^{\text{s}}(\gamma)$ accounts for the dependence on the specific heat ratio γ , the indicator of the thermal evolution. At

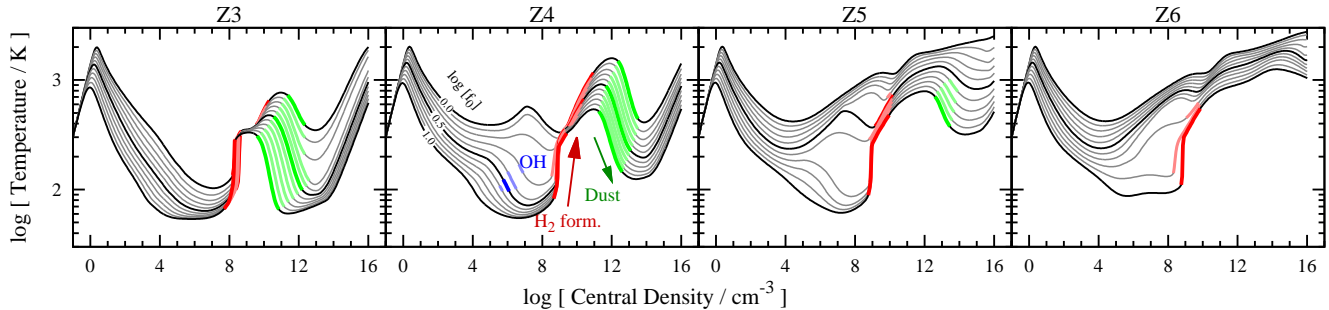


Figure 10. Temperature as a function of the density in a cloud core obtained by the semi-analytic chemo-thermal evolution model of gas clouds for Z3–6 from left to right with f_0 (defined as Equation 3) from 1 to 10 every 0.5 dex (thick curves) and every 0.1 dex (thin curves). We also draw thick and colored segments in the regimes where $\gamma > 1.1$ by H_2 formation heating (red), where $\gamma < 0.7$ by OH and H_2O cooling (blue), and where $\gamma < 0.8$ by dust emission (green) on each evolutionary track.

$\gamma > 0$, gas clouds undergo inhomogeneous collapse, and the pressure gradient force delays collapse with respect to the collapse time $t_{\text{col}}^s(0)$ in the limit of $\gamma \rightarrow 0$ as

$$t_{\text{col}}^s(\gamma) = \frac{1}{\sqrt{1 - f_p(\gamma)}} t_{\text{col}}^s(0), \quad (4)$$

where $f_p(\gamma)$ is the ratio of pressure gradient force to gravitational force (Larson 1969). In this limit, the cloud dynamics becomes practically identical with the dust collapse, in which the pressure is uniformly zero. The collapse time asymptotically approaches $t_{\text{col}}^s(0) = (2/3\pi)t_{\text{ff}} = 0.21t_{\text{ff}}$, where $t_{\text{ff}} = (3\pi/32G\rho)^{1/2}$ is the free-fall time at mass density ρ (Penston 1969). The ratio $f_p(\gamma)$ can be derived from the self-similar solution of spherical clouds with polytropic equation of state. Omukai et al. (2005) present the fitting formula as

$$f_p(\gamma) = \begin{cases} 0, & (\gamma < 0.83) \\ 0.6 + 2.5(\gamma - 1) - 6.0(\gamma - 1)^2, & (0.83 < \gamma < 1) \\ 1.0 + 0.2(\gamma - 4/3) - 2.9(\gamma - 4/3)^2, & (\gamma > 1) \end{cases} \quad (5)$$

Hereafter, we utilize the parameter f_0 to represent the bulk rate of the cloud collapse.

4.4.1 One-zone semi-analytic model

It is costly to run additional three-dimensional simulations which cover a large parameter regions of Z and f_0 . We thus resort to utilizing a simpler approach focusing on the chemo-thermal evolution of a cloud. To this aim, the semi-analytic one-zone model of C15 is suitable. We modify the code such that the density in the cloud center increases according to

$$\frac{d\rho}{dt} = \frac{\rho}{t_{\text{col}}} = \frac{\rho}{f_0 t_{\text{col}}^s(\gamma)} \quad (6)$$

with various f_0 .³ With $\gamma \rightarrow 4/3$, the collapse time $t_{\text{col}}^s(\gamma)$ diverges. Our simulations show that the clouds continues to collapse by accreting ambient gas even with $\gamma > 4/3$. To mimic this, we set the upper limit of $f_p(\gamma)$ as 0.95. For given

density and temperature, our one-zone code solves exactly the same chemical reactions including grain growth and gas heating/cooling processes as in our three-dimensional simulations. The CMB temperature is set to be 50 K (redshift ~ 20). We perform the calculations with varying $f_0 = 1\text{--}10$ every 0.05 dex and $Z = 10^{-6}\text{--}10^{-3} Z_{\odot}$ every 0.1 dex to cover the parameter range of early clouds.

Figure 10 shows the temperature evolution of the cloud center with various values f_0 from 1 to 10 every 0.1 dex. The gas temperature monotonically decreases with increasing f_0 at each density. We find that the evolution track for our simulated clouds (Figure 6) follows closely one of the black curves in Figure 10 with a corresponding f_0 shown in Table 3. We indicate by thick colored segments the regimes where we can identify important thermal processes that determine the cloud elongation and fragmentation. Extending the approach of Schneider & Omukai (2010), we from our simulations define the threshold value of specific heat ratio γ_{th} below/above which cooling/heating makes cloud elongated/round.

The gas cloud can fragment if the cloud ellipticity is sufficiently large in advance to the rapid gas cooling. In our simulations, γ decline down only to 0.84 and 0.85 for UNI and MH2 Z5, respectively, while down to 0.78 for MH1 Z5 (see middle panels of Figure 6). The critical $\gamma_{\text{th}}^{\text{dust}}$ for dust-induced fragmentation can be defined as 0.8. The green segments in Figure 10 represent the regime where dust cooling is efficient to reduce γ down to 0.8.

The condition is not met if the trajectory passes through the regime colored in red, where significant H_2 formation heating processes. Figure 6 shows that the γ increases larger than 1.1. Although γ exceed 1.1 for UNI Z3, the strong turbulence ($\varepsilon_{\text{turb}} = 0.350$) as well as significant dust cooling efficiency might induce fragmentation. Let us define the threshold $\gamma_{\text{th}}^{\text{H}_2}$ as 1.1 for H_2 formation heating to halt fragmentation. In Figure 10, the red segments are plotted in the regime where γ exceeds 1.1 due to hydrogen molecular formation.

In the limited cases with metallicity $10^{-4} Z_{\odot}$, we find that the OH cooling, which is efficient in the blue-colored regions at $n_{\text{H}} \sim 10^7 \text{ cm}^{-3}$, can prevent the gas cloud from recovering a round shape. Although γ reaches down to 0.41

³ C15 investigate the cloud evolution only in the case with $f_0 = 3\pi/2 = 4.7$ (also see Larson 1969; Omukai et al. 2010).

Table 3. Collapse timescale of clouds f_0 .

$Z [Z_\odot]$	UNI	MH1	MH2	MH3
10^{-3}	1.1 ± 0.4	1.7 ± 0.6	2.4 ± 2.0	3.6 ± 2.1
10^{-4}	1.1 ± 0.4	2.2 ± 0.9	2.4 ± 1.6	5.4 ± 3.4
10^{-5}	1.0 ± 0.3	2.1 ± 0.6	2.0 ± 1.8	6.2 ± 3.2
10^{-6}	1.0 ± 0.2	2.0 ± 0.5	2.1 ± 1.8	6.4 ± 3.4

Note — To compute f_0 for the simulated clouds, we measure the collapse time as $t_{\text{col}} = \rho/(\Delta\rho/\Delta t)$ at each output time with $10^2 < n_{\text{H,peak}} < 10^8 \text{ cm}^{-3}$. We then take the arithmetic mean and the standard deviation of f_0 .

at density $n_{\text{H}} = 4 \times 10^6 \text{ cm}^{-3}$ in our simulation (for MH1 Z4), it never decreases down to 0.7 in our one-zone calculations. It would be the limitation of the one-zone model. Since the threshold $\gamma_{\text{th}}^{\text{OH}}$ for OH cooling has an uncertainty, we search $\gamma_{\text{th}}^{\text{OH}}$ which reproduce the simulation results. In Figure 6, we show the area with $\gamma_{\text{th}}^{\text{OH}} = 0.7$ as blue-colored segments. As the simulations with metallicity $10^{-4} Z_\odot$ indicate, γ becomes below $\gamma_{\text{th}}^{\text{OH}}$ with a limited range of f_0 . The cloud passes the regime where OH cooling is efficient in the range $f_0 \simeq 2.5\text{--}4.5$.

We present the results of all our model calculations in Figure 11. The green- and blue-shaded regions indicate the regime where fragmentation criteria are satisfied. There, we also mark the results of our three-dimensional simulations (Table 3). The models that result in fragmentation is indicated by filled symbols, and otherwise by open symbols. The parameter regions for the fragmentation defined by the semi-analytic model are qualitatively consistent with the results of the simulations with $10^{-5}\text{--}10^{-4} Z_\odot$. The result for UNI Z3 can not be reproduced, but this may reflect simply the limitation of our one-zone model to represent the non-linear evolution of hydrostatic core formed by H_2 formation heating.

In Figure 11, the green, red, and blue lines correspond to the boundaries between the models where dust cooling, chemical heating, and molecular cooling, respectively, are effective and not. To draw the boundary curves, we linearly interpolate the critical f_0 and Z obtained by the one-zone calculations. Above the green-dotted line, dust cooling can trigger gas fragmentation (criterion *i*). Below the red-dashed line, H_2 formation heating is not effective to suppress the gas elongation (*ii-a*). In the regions surrounded by the blue solid lines, OH and H_2O cooling can enhance the cloud elongation even though the H_2 formation heating is effective above the red-dashed line (*ii-b*). The green-shaded region indicates the parameter region where the criteria (*i*) and (*ii-a*) are both satisfied. In the blue-shaded regions, the fragmentation is favored by the OH and H_2O cooling. Interestingly, our criteria are satisfied in the limited metallicity region $Z \sim 10^{-5}\text{--}10^{-4} Z_\odot$. In the next section, we explain and derive the boundaries using simple analytic models.

4.4.2 Analytic formulae of the boundaries

Dust cooling

The criterion (*i*) is defined by the balance between the compressional heating rate Γ_{adi} and the rate of heat transfer from gas to dust, Λ_{d} . In C15, we define the criterion of

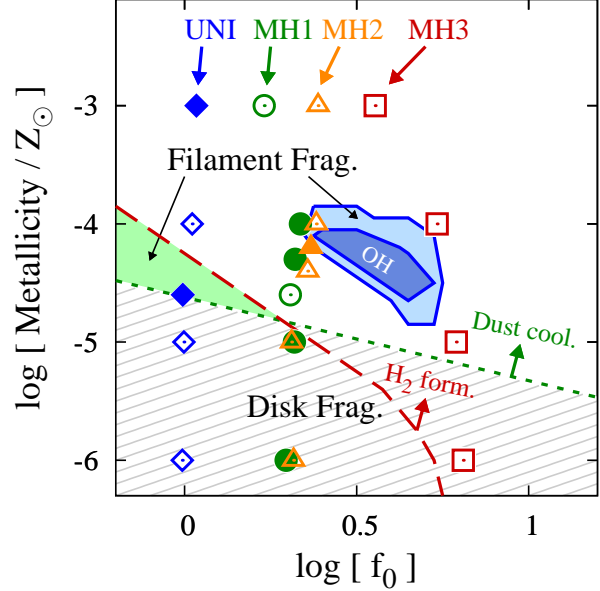


Figure 11. We plot the regions of the collapse timescale f_0 and the metallicity Z favourable for the filament fragmentation (green- and blue- shaded regions) and for the disk fragmentation (grey-hatched region). Dust cooling is efficient in the region above the green dashed lines (labeled “Dust cool.”). H_2 formation heating is efficient in the region above the red dotted lines (“ H_2 form.”). OH and H_2O cooling is efficient in the region surrounded by blue solid line (“OH”). We draw the lines for the threshold specific heat ratios $\gamma_{\text{th}}^{\text{OH}} = 0.65$ (blue) and 0.70 (cyan) above which OH cooling is regarded to promote sufficiently (see text). We define these lines by linear interpolation of the results of the semi-analytic calculations with varying $f_0 = 1\text{--}10$ every 0.05 dex and $Z/Z_\odot = 10^{-6}\text{--}10^{-3}$ every 0.1 dex. We also over-plot f_0 and Z of the simulated clouds UNI (blue diamonds), MH1 (green circles), MH2 (orange triangles), and MH3 (red squares). Open and close symbols indicate the models that end with and without fragments, respectively.

metallicity for efficient dust cooling as

$$Z > 10^{-5.5} Z_\odot \left(\frac{f_{\text{dep},0}}{0.18} \right)^{-0.44}.$$

The equation is defined with $f_0 = 3\pi/2 = 4.7$. Since $\Gamma_{\text{adi}} = p/t_{\text{col}}$ is reciprocally proportional to f_0 , the more general formula of this criterion is

$$Z > 10^{-5.5} Z_\odot \left(\frac{f_{\text{dep},0}}{0.18} \right)^{-0.44} \left(\frac{f_0}{4.7} \right)^{-1}.$$

Since it is unrealistic to measure the mass fraction of all heavy elements, we convert this equation to

$$10^{[\text{Mg}/\text{H}]} > 1.5 f_0^{-1} \left(\frac{f_{\text{dep},0}}{0.18} \right)^{-0.44} \times 10^{-5}, \quad (7)$$

using abundance of magnesium as a reference element. In this conversion, we use the relationship $10^{[\text{Mg}/\text{H}]} = Z/Z_\odot$.⁴

⁴ Indeed, our Pop III nucleosynthesis models predict that $10^{[\text{Mg}/\text{H}]} = [0.86\text{--}1.21](Z/Z_\odot)$ for core-collapse supernovae (CC-SNe) with progenitor mass $M_{\text{pr}} = 13\text{--}30 M_\odot$, and $10^{[\text{Mg}/\text{H}]} =$

Cayrel et al. (2004) suggests that Mg would be more suitable as the reference element to stellar metallicity than Ca and Fe because its main production epoch is hydrostatic burning of progenitor stars, and because its abundance is less affected by mixing/fallback mechanism of SN (Woosley & Weaver 1995). Also, magnesium is the key element of forsterite (Mg_2SiO_4) grains, which is main species for gas cooling for most Pop III SN models (C15), i.e., magnesium controls the abundance of forsterite grains because its stoichiometric number is two. Therefore, we use magnesium as a reference species.

H₂ formation heating

The condition where the rapid gas heating by H₂ formation occurs is that the equilibrium temperature T_{eq} at $n_{\text{H}} < 10^8 \text{ cm}^{-3}$ is smaller than that at $n_{\text{H}} > 10^8 \text{ cm}^{-3}$. At 10^{11} cm^{-3} , the thermal balance between H₂ formation heating and H₂ line cooling yields $T_{\text{eq}} \sim 870 \text{ K}$. At $n_{\text{H}} = 10^7 \text{ cm}^{-3}$, adiabatic gas compression is a major heating process, whereas the dominant cooling mechanism is H₂ line transition with $Z \lesssim 10^{-5} Z_{\odot}$, or H₂O line transition with $Z \gtrsim 10^{-5} Z_{\odot}$. The condition where the equilibrium temperature is less than 870 K at $n_{\text{H}} = 10^7 \text{ cm}^{-3}$ is $\Gamma_{\text{adi}} < \Lambda_{\text{H}_2} + \Lambda_{\text{H}_2\text{O}}$, where Λ_x is the cooling rate of species x per unit volume. Since oxygen is almost fully in the form of H₂O molecules at this density, these cooling and heating rates are given by

$$\Gamma_{\text{adi}} = 2.8 \times 10^{-17} f_0^{-1} \text{ erg cm}^{-3} \text{ s}^{-1},$$

$$\Lambda_{\text{H}_2} = 3.7 \times 10^{-18} \text{ erg cm}^{-3} \text{ s}^{-1},$$

$$\Lambda_{\text{H}_2\text{O}} = 4.0 \times 10^{-18} \left(\frac{10^{[\text{O}/\text{H}]}}{10^{-5}} \right) \text{ erg cm}^{-3} \text{ s}^{-1}$$

at 10^7 cm^{-3} and $T = 870 \text{ K}$ with $t_{\text{col}}^s(1.0) = 0.34t_{\text{ff}}$. Thus, using oxygen abundance, we can write the condition as

$$10^{[\text{O}/\text{H}]} > (6.8f_0^{-1} - 0.91) \times 10^{-5}. \quad (8)$$

The boundary is consistent with the red dashed line in Figure 11. For a gas cloud with f_0 and Z above both the red and green lines, we expect that the gas does not get elongated owing to the effect of rapid H₂ formation heating. Hence the filament fragmentation does not occur either when dust cooling is effective. On the other hand, the green shaded region above the green line and below the red line is the regime where the dust cooling is efficient but H₂ formation heating is not (criteria *i* and *ii-a*). The cloud MH1 Z5 where the fragmentation occurs is plotted in the green region. We explicitly confirm the cloud fragmentation in the additional simulation for UNI with $10^{-4.6} Z_{\odot}$.

OH and H₂O cooling

The region surrounded by the blue solid lines indicate the regime where OH and H₂O cooling is effective. At $n_{\text{H}} \sim 10^7 \text{ cm}^{-3}$, OH cooling rate exceeds the compressional heating rate. The rates are

$$\Gamma_{\text{adi}} = 1.0 \times 10^{-17} f_0^{-1} \text{ erg cm}^{-3} \text{ s}^{-1},$$

1.12 and $0.84(Z/Z_{\odot})$ for pair-instability supernovae (PISNe) with $M_{\text{pr}} = 170$ and $200 M_{\odot}$, respectively.

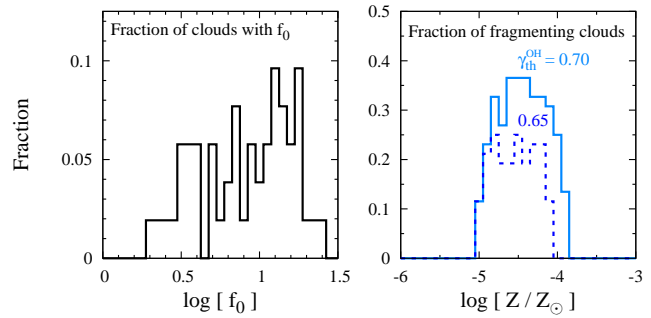


Figure 12. *Left panel:* number of 52 Pop III clouds with various collapse time f_0 simulated by H14. *Right panel:* number fraction of Pop II clouds which will undergo fragmentation if these clouds have the same f_0 distribution as Pop III clouds. We integrate the fraction of clouds with f_0 which satisfy the fragmentation condition defined by the one-zone calculations. The frequency depends on the threshold specific heat ratio $\gamma_{\text{th}}^{\text{OH}}$ below which cloud is considered to be elongated sufficiently by OH cooling. We consider two cases with $\gamma_{\text{th}}^{\text{OH}} = 0.65$ (blue) and 0.70 (cyan).

$$\Lambda_{\text{OH}} = 1.2 \times 10^{-18} \left(\frac{10^{[\text{O}/\text{H}]}}{10^{-4}} \right) \text{ erg cm}^{-3} \text{ s}^{-1}$$

at 10^7 cm^{-3} and 200 K with $t_{\text{col}}^s(0.5) = 0.21t_{\text{ff}}$, where OH abundance is in general a tenth of oxygen abundance. The condition where $\Gamma_{\text{adi}} = \Lambda_{\text{OH}}$ can be derived to be

$$10^{[\text{O}/\text{H}]} = 1.6f_0^{-1} \times 10^{-4}. \quad (9)$$

For large f_0 and Z , OH molecules are formed at $n_{\text{H}} < 10^7 \text{ cm}^{-3}$ and Γ_{adi} balances Λ_{OH} already at 10^7 cm^{-3} . In this case, the gas evolves nearly isothermally without significant temperature drop. Therefore, the condition (*ii-b*) is satisfied in the narrow region around the part of the line given by Equation (9). The blue shaded region with the label “OH/H₂O” indicate the regimes where OH and H₂O cooling promotes the gas elongation. For the combination of f_0 and Z in these regions, the gas cloud eventually fragments by dust cooling even though H₂ formation heating is efficient (criteria *i* and *ii-b*). The cloud MH1 Z4 (discussed in Section 4.3.3) is in the blue-shaded region, where the OH cooling enhances gas elongation (Figure 6), and gas fragmentation is finally triggered (Figure 5). Also for MH2 with $10^{-4.2} Z_{\odot}$, the clouds are sufficiently elongated to fragment.

4.4.3 Fraction of low-mass star-forming clouds

It is interesting to ask the number fraction of the clouds that yield fragments. In order to know this, a distribution of the collapse timescale of low-metal gas clouds is needed. Unfortunately, we can not observationally derive the statistics of the collapse timescale of clouds. Instead, one of the clues may be obtained from the distribution of the collapse timescales of primordial clouds obtained by the cosmological simulations of H14. We derive f_0 for 52 primordial clouds. The left panel of Figure 12 shows the distribution of f_0 of primordial clouds. It spreads between $\log(f_0) = 0.3$ and 1.4 . We then calculate the number fraction of clouds that satisfy our fragmentation criterion indicated in Figure 11 with different metallicities. The right panel of Figure 12 shows the number fraction of Pop II clouds which will undergo

fragmentation. The fraction depends on the threshold value of specific heat ratio $\gamma_{\text{th}}^{\text{OH}}$ under which OH cooling can enhance cloud elongation (see Section 4.4.2). We consider the two cases with $\gamma_{\text{th}}^{\text{OH}} = 0.65$ and 0.70 . For severer criterion, $\gamma_{\text{th}}^{\text{OH}} = 0.65$, the fraction becomes systematically smaller. For 10^{-5} – $10^{-4} Z_{\odot}$, the fractions are predicted to be ~ 25 and 35% for $\gamma_{\text{th}}^{\text{OH}} = 0.65$ and 0.70 , respectively. It has been considered that clouds would be more likely to host low-mass stars with increasing metallicity. However, we find that H_2 formation heating can prohibit fragmentation in a range of metallicity $\gtrsim 10^{-4} Z_{\odot}$. In our model, we predict that the metallicity range between $\sim 10^{-5}$ and $\sim 10^{-4} Z_{\odot}$ is favored to fragmentation. Even in this range, clouds which undergo fragmentation is minority. Considering that we here employ the carbon-normal elemental abundance ($[\text{C}/\text{Fe}] < 1$), we argue that the number of low-mass EMP stars discovered so far is small (Caffau et al. 2011b), possibly reflecting the stringent constraints on the fragmentation of low-metallicity gas clouds. Here we estimate the fraction of clouds with fragmentation with the elemental abundance of Pop III progenitor with $30 M_{\odot}$. In Section 5, we see the metal abundances with which fragmentation occurs for a wide range of progenitor masses.

4.5 Disk fragmentation with $Z \lesssim 10^{-5} Z_{\odot}$

The fragmentation occurs also for MH1 Z6 although its f_0 and Z are outside the region of the fragmentation condition shown in Figure 11. That is even reasonable because the criteria should not be applied to the cases with

$$Z < 1.5 f_0^{-1} \left(\frac{f_{\text{dep},0}}{0.18} \right)^{-0.44} \times 10^{-5} Z_{\odot}, \quad (10)$$

where dust cooling is inefficient (see Equation 7). Several authors have discussed that low-mass stars are likely to form by the fragmentation on the accretion disks even in the metal-free cases (Clark et al. 2011; Greif et al. 2012; Susa et al. 2014). It can be considered that the fragmentation in their simulations can be categorized in the disk fragmentation.

In the regime, the fragmentation is not triggered by gas cooling but would be triggered by its self-gravity (e.g. Vorobyov & Basu 2010). Gravitational instability of a protostellar disk has been studied extensively (e.g. Gammie 2001). In our simulations, the cloud fragments only for one cloud MH1 Z6 out of five clouds (UNI Z5 and four Z6 clouds) satisfying Equation (10). It might be because of the peculiar density distribution of the MH2 cloud or just because the disk evolution can be followed for the longest time (16 years) among the five clouds. The fragmentation might be observed also for other clouds if we could follow their evolutions for the longer time. Here, we indicate the maximal region favorable to the disk fragmentation as Equation (10) indicated by the grey-hatched area on the f_0 - Z plane of Figure 11.

In our cloud MH1 Z6, five gas clumps are formed but all of them immediately migrate into the central primitive protostar with a life time of several years. If the formation and migration continue similarly, the mass of the central protostar quickly increases. If some blobs are ejected from the dense disk by multi-body dynamical interactions, they would avoid the merger with the central star and also could no longer accrete the gas from the disk (Zhu et al. 2012;

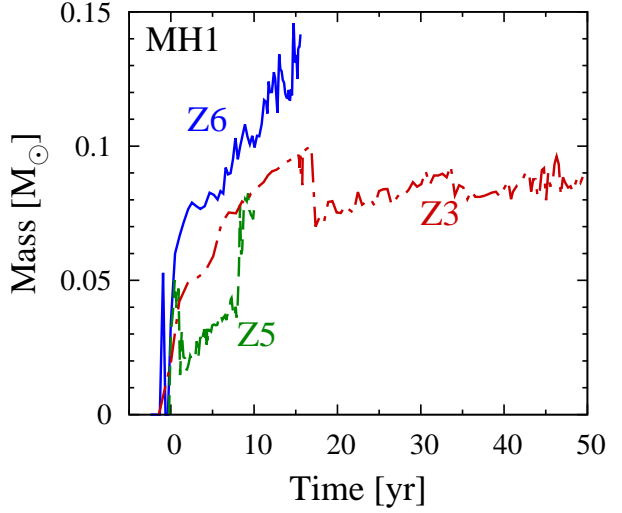


Figure 13. Mass of the protostar first formed in the cloud MH1 for Z3 (red dot-dashed), Z5 (green dashed), and Z6 (blue solid) as a function of the time from the formation of the first protostar.

Susa et al. 2014). This would lead the formation of the low-mass stars even in the so-called “hyper metal-poor (HMP)” regime with metallicities $\lesssim 10^{-5} Z_{\odot}$.

5 DISCUSSION AND CONCLUSION

5.1 Summary

The most important conclusion we draw from our set three-dimensional simulations is that not only the gas metallicity Z but also the collapse timescale f_0 determine the thermal evolution and fragmentation “mode” of a contracting gas cloud. Thermal evolution and core fragmentation are intrinsically connected to each other in the following manner:

- The dust thermal emission induces significant deformation of a cloud core. Because accretion of gas-phase metal onto grains enhances cooling efficiency, it is important to follow the growth of dust grains in a low-metallicity gas.
- Gas heating by H_2 formation via three-body reactions plays a crucial role to halt the elongation of the gas in the cases of vast majority with metallicities 10^{-4} – $10^{-3} Z_{\odot}$ with the early metal and dust model.
- OH and H_2O gas cooling enhances the cloud elongation and yields favorable conditions for core fragmentation later when dust cooling becomes efficient. In some cases, this occurs before H_2 formation heating becomes efficient.

We can qualitatively explain the conditions of filamentary fragmentation on a f_0 - Z plane as shown in Figure 11.

5.2 Origin of f_0

The difference of cloud collapse time would result from the depth of potential well created by hosting dark matter halos. We find that the depth $GM_{\text{vir}}/R_{\text{vir}}$ (Table 1) negatively correlates with the collapsing time f_0 for the 52 primordial clouds including MH1, MH2, and MH3 simulated by H14. This shows that, as the potential well becomes deeper, the

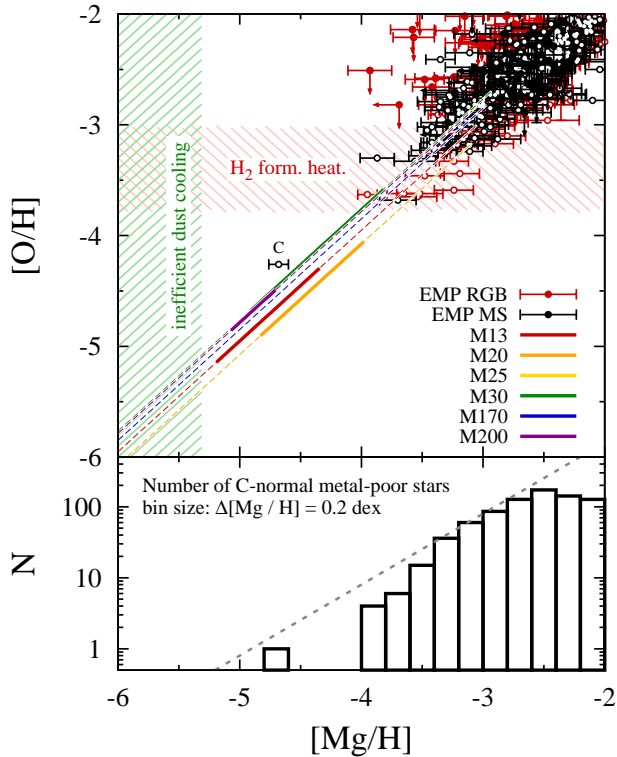


Figure 14. *Top panel:* magnesium and oxygen abundances with which the relevant thermal processes affect the cloud fragmentation. The green colored line represents the combination of Mg and O abundances predicted by the Pop III core-collapse supernova (CCSN) model with progenitor mass $M_{\text{pr}} = 30 M_{\odot}$ employed in our simulations. We also draw the abundances synthesized in CCSNe with $M_{\text{pr}} = 13, 20,$ and $25 M_{\odot}$ by the red, orange, and yellow lines, respectively. The blue and purple lines are for pair-instability supernova (PISN) models respectively with $M_{\text{pr}} = 170$ and $200 M_{\odot}$. These lines are drawn up to the metallicity $Z = 10^{-3} Z_{\odot}$, above which a single SN explosion can hardly enrich clouds (e.g. Audouze & Silk 1995). Our one-zone model predicts that the fragmentation occurs in the solid segment for *existing* f_0 , while not in the dashed region for *any* f_0 (with a range of $f_0 = 1$ – 10). In the green-hatched region, dust cooling is ineffective because the abundance of magnesium (key element of silicate grains) is too small (Equation 7). In the red-hatched region, rapid H_2 formation heating halts cloud elongation because temperature declines by H_2O molecular cooling before the exothermic reactions of H_2 formation sets in (Equation 8). We also plot the abundances of the extremely metal-poor (EMP) stars so far observed for comparison taken from the SAGA database (Suda et al. 2008, <http://sagadatabase.jp/>). The open circles represent the stars whose oxygen abundance is unavailable, and predicted from iron abundance with the average rate $[\text{O}/\text{Fe}] = 0.47$ of the EMP stars (Cayrel et al. 2004). The star labeled “C” is most metal-poor star ever observed, SDSS J102915 + 172927 (Caffau et al. 2011b). *Bottom panel:* histogram of the magnesium abundances of EMP stars with bin size of $\Delta[\text{Mg}/\text{H}] = 0.2$ dex. The dashed black line shows the reciprocal relationship of star formation to gas metallicity predicted by a simple cosmological enrichment model by (Hartwick 1976).

collapse time becomes shorter. We also find that gas rotation hardly affects the collapse timescale.

5.3 Comparison with the observations

In our simulation, we employ the progenitor model only with mass $M_{\text{pr}} = 30 M_{\odot}$ and ambient gas density $n_{\text{amb}} = 1 \text{ cm}^{-3}$. In this progenitor model, we have seen that oxygen and magnesium can control the cooling/heating rates important for the cloud fragmentation (Section 4.4.2). The combination of Mg and O abundances are drawn by the green line in Figure 14. Our one-zone calculations show that f_0 for which the cloud would fragment *exists* with metallicities $-5.0 < \log(Z/Z_{\odot}) < -3.9$ (Figure 11). This region is shown by the solid thick segment in Figure 14. Similarly, the region of Mg and O abundances for other core-collapse supernova (CCSN) models with $M_{\text{pr}} = 13, 20,$ and $25 M_{\odot}$ and pair-instability supernova (PISN) models with $M_{\text{pr}} = 170$ and $200 M_{\odot}$ is shown by red, yellow, orange, blue, and purple lines, respectively, in Figure 14. These lines are drawn up to the corresponding metallicity $Z = 10^{-3} Z_{\odot}$, above which a single SN can hardly enrich a cloud, i.e., our assumption that the cloud is polluted by a single SN would fail (Audouze & Silk 1995).

For progenitor masses $M_{\text{pr}} = 20$ (orange) and $200 M_{\odot}$ (purple), $\text{OH}/\text{H}_2\text{O}$ cooling operates as in the case with $M_{\text{pr}} = 30 M_{\odot}$. For $M_{\text{pr}} = 13 M_{\odot}$, the molecular cooling can not affect the cloud fragmentation because oxygen is less abundant ($\text{C}/\text{O} > 1$). Instead, carbon grains can grow and contribute to fragmentation. For $M_{\text{pr}} = 25 M_{\odot}$ (yellow), since $\text{C}/\text{O} < 1$, carbon grains can not grow to enhance cloud fragmentation. Nevertheless, since the ratio C/O is still less than $M_{\text{pr}} = 20$ and $30 M_{\odot}$ models (also see Nozawa et al. 2003), cooling and silicate grains is not important. In PISN case with $M_{\text{pr}} = 170 M_{\odot}$ (blue), silicate grains have already been significantly destroyed by the reverse shock just after the explosion. In the models with $M_{\text{pr}} = 25$ and $170 M_{\odot}$, even the criterion (i) is not satisfied for any $f_0 = 1$ – 10 .

In the most cases of carbon-normal star formation, we could say that Mg and O abundances are important to predict the fragmentation property of the prestellar clouds. Instead, the fragmentation of carbon-enhanced cloud should be controlled by other factors such as carbon abundance (see Marassi et al. 2014). Even in our progenitor model with $M_{\text{pr}} = 13 M_{\odot}$, we see that the C I cooling creates the steep temperature decline. Whether this decline can enhance the cloud elongation or not can not be determined by the one-zone model. We will discuss this in the forthcoming paper.

The one-zone model predicts the region where cloud fragmentation is disfavored because dust cooling is insufficient by a small amount of magnesium is shown by the green-hatched region in Figure 14. In the red-hatched region, cloud elongation is prevented by H_2 formation heating. With metallicities $Z \gtrsim 10^{-3} Z_{\odot}$, the abundance ratio approaches the present-day value ($[\text{O}/\text{H}] = [\text{Mg}/\text{H}]$), and the dust properties would also approach the one in the local interstellar medium. If so, we can predict that H_2 formation heating would prevent fragmentation in the range $-4 \lesssim [\text{O}/\text{H}] \lesssim -3$.

Figure 14 also shows the magnesium and oxygen abundances of EMP stars so far observed by filled circles. Unfortunately, oxygen abundance of considerable stars is unavail-

able because the oxygen line is generally under the detection limit or blended with the telluric lines (Cayrel et al. 2004). To secure the statistical samples, we resort to iron abundance of some EMP stars whose oxygen abundance is not detected. We convert the iron abundance to oxygen abundance, using the “typical” ratio $[\text{O}/\text{Fe}] = 0.47$ (Cayrel et al. 2004).⁵ These abundances are shown by open circles in Figure 14. In the bottom panel of Figure 14, we show the frequency of the magnesium abundance of EMP stars.

The observations have so far found no EMP stars in the green region where dust cooling fails. Also, the less number of stars are found in the red-hatched region where H_2 formation heating is promoted. The simple enrichment model of Hartwick (1976) suggests that the star formation rate is reciprocally proportional to the metallicity. The departure of the observed frequency (black boxes in Figure 11) from the predicted reciprocal relationship (black dashed line) below the metallicity $\sim 10^{-3.5} Z_\odot$ might be owing to the effect of H_2 formation heating (also see Tsuribe & Omukai 2008). Also, the abundance of the star SDSS J102915 + 172927 (labeled by “C”) is not inconsistent with the isolated region favorable to cloud fragmentation drawn by solid lines. Both further model predictions and observations should be required to give a determinative conclusion for the origin of the EMP and low-mass stars in the Galactic halo.

5.4 Other important physics

It is important to notice that the formation of low-mass fragments does not immediately suggest the formation of low-mass, low-metallicity stars. The final mass of a star is determined when its protostellar evolution reaches the zero-age main sequence, i.e., after the whole history of gas accretion from the circumstellar disk starting from a tiny embryo through growth and contraction (Shu 1977, 1978; Omukai & Palla 2003; Hosokawa et al. 2011, 2012). Since the dynamical time becomes progressively small with increasing density as $\propto \rho^{-1/2}$, we are able to follow the gas accretion process only several decades after the first protostar formation because of technical difficulties. There are a number of important physical processes that affects the growth of a protostar after the initial phase. For example, when the first, central protostar grows to $\sim 10 M_\odot$, photodissociation and photoionization by the ultraviolet emission may become effective to suppress the gas accretion onto the central star (Hosokawa et al. 2012). The magnetic field would also affect the accretion process (Machida & Doi 2013).

We follow the gas accretion onto protostars for a limited time (a few tens of years) after the first protostar is formed because we do not employ the sink-particle technique. However, we can accurately follow the process of the gas accretion including the merger of protostellar cores. We plot the accretion history of the central protostar for MH1 in Figure 13. As for the other clouds, we find that the protostar accretes a larger amount of gas with lower metallicities. We also comment that the mass accretion rate onto the protostar for MH1 is smaller than for UNI and MH2 even with the same metallicity. This is because the gas temperature

remains lower in a slowly contracting gas cloud. Furthermore, the accreting gas is shared by several fragments, and the growth rate of each core is correspondingly reduced. One can naively guess that the fraction of low-mass stars would increase with increasing metallicity.

In a realistic case where the gas is directly enriched by Pop III SNe, significant turbulence would be generated. Turbulence can suppress the growth of density perturbations, or rather can even promote gas fragmentation (Dopcke et al. 2011, 2013; Smith et al. 2015). Dopcke et al. (2013) report that small mass fragments (sink-particles) are formed in turbulent gas for a wide range of metallicities from 0 to $10^{-3} Z_\odot$. They also find that the mass function of sink particles transforms from flat one to bottom-heavy with increasing metallicities between 10^{-5} and $10^{-4} Z_\odot$. Smith et al. (2015) find vigorous fragmentation of a gas that is enriched with a metallicity $2 \times 10^{-5} Z_\odot$ by the Pop III SN exploding on a neighboring halo. Their result supports the notion that turbulence-driven disturbances in a low-metallicity gas induce gas fragmentation. It is still uncertain how the sink particle technique employed in their simulations would affect the fragmentation properties. Further studies are certainly needed to examine the effects of turbulence on gas fragmentation in a fully cosmological set up.

ACKNOWLEDGMENTS

We thank K. Omukai for fruitful discussion. The Pop III dust model is calculated by T. Nozawa. We could make our manuscript highly improved by the anonymous referee’s comments. GC and SH are supported by Research Fellowships of the Japan Society for the Promotion of Science (JSPS) for Young Scientists. NY acknowledges the financial supports from JST CREST and from JSPS Grant-in-Aid for Scientific Research (25287050). The numerical simulations are carried out on Cray XC30 at Center for Computational Astrophysics, National Astronomical Observatory of Japan and on COMA at Center for Computational Sciences in University of Tsukuba.

REFERENCES

- Aoki, W., Tominaga, N., Beers, T. C., Honda, S., & Lee, Y. S. 2014, *Science*, 345, 912
- Audouze, J., & Silk, J. 1995, *ApJ*, 451, L49
- Bovino, S., Grassi, T., Schleicher, D. R. G., & Banerjee, R. 2016, arXiv:1601.04525
- Bromm, V., Ferrara, A., Coppi, P. S., & Larson, R. B. 2001, *MNRAS*, 328, 969
- Bromm, V., & Loeb, A. 2003, *Nat*, 425, 812
- Bullock, J. S., Dekel, A., Kolatt, T. S., et al. 2001, *ApJ*, 555, 240
- Caffau, E., Ludwig, H. G., Steffen, M., Freytag, B., & Bonifacio, P. 2011, *Sol. Phys.*, 268, 255
- Caffau, E., Bonifacio, P., François, P., et al. 2011, *Nature*, 477, 67
- Caffau, E., Bonifacio, P., François, P., et al. 2012, *A&A*, 542, A51
- Cayrel, R., Depagne, E., Spite, M., et al. 2004, *A&A*, 416, 1117

⁵ The rate $[\text{O}/\text{Fe}]=0.47$ is obtained from 3D stellar atmosphere model. The 1D model predicts $[\text{O}/\text{Fe}] = 0.7$.

- Clark, P. C., Glover, S. C. O., Smith, R. J., et al. 2011, *Science*, 331, 1040
- Chiaki, G., Nozawa, T., & Yoshida, N. 2013, *ApJ*, 765, L3
- Chiaki, G., Marassi, S., Nozawa, T., et al. 2015, *MNRAS*, 446, 2659
- Chiaki, G., & Yoshida, N. 2015, *MNRAS*, 451, 3955
- Dopcke, G., Glover, S. C. O., Clark, P. C., & Klessen, R. S. 2011, *ApJ*, 729, L3
- Dopcke, G., Glover, S. C. O., Clark, P. C., & Klessen, R. S. 2013, *ApJ*, 766, 103
- Frebel, A., Aoki, W., Christlieb, N., et al. 2005, *Nat*, 434, 871
- Gammie, C. F. 2001, *ApJ*, 553, 174
- Geha, M., Brown, T. M., Tumlinson, J., et al. 2013, *ApJ*, 771, 29
- Grassi, T., Bovino, S., Haugboelle, T., & Schleicher, D. R. G. 2016, arXiv:1606.01229
- Greif, T. H., Springel, V., White, S. D. M., et al. 2011, *ApJ*, 737, 75
- Greif, T. H., Bromm, V., Hanawa, T., & Matsumoto, T. 2000, *PASJ*, 52, 241
- Hartwick, F. D. A. 1976, *ApJ*, 209, 418
- Hartwig, T., Bromm, V., Klessen, R. S., & Glover, S. C. O. 2015, *MNRAS*, 447, 3892
- Hosokawa, T., Omukai, K., Yoshida, N., & Yorke, H. W. 2011, *Science*, 334, 1250
- Hosokawa, T., Omukai, K., & Yorke, H. W. 2012, *ApJ*, 756, 93
- Hollenbach, D., & McKee, C. F. 1979, *ApJS*, 41, 555
- Hirano, S., & Yoshida, N. 2013, *ApJ*, 763, 52
- Hirano, S., Hosokawa, T., Yoshida, N., et al. 2014, *ApJ*, 781, 60
- Hirano, S., Hosokawa, T., Yoshida, N., Omukai, K., & Yorke, H. W. 2015, *MNRAS*, 448, 568
- Inutsuka, S.-I., & Miyama, S. M. 1997, *ApJ*, 480, 681
- Ishiyama, T., Sudo, K., Yokoi, S., et al. 2016, arXiv:1602.00465
- Jappsen, A.-K., Glover, S. C. O., Klessen, R. S., & Mac Low, M.-M. 2007, *ApJ*, 660, 1332
- Jappsen, A.-K., Klessen, R. S., Glover, S. C. O., & Mac Low, M.-M. 2009, *ApJ*, 696, 1065
- Jappsen, A.-K., Mac Low, M.-M., Glover, S. C. O., Klessen, R. S., & Kitsionas, S. 2009, *ApJ*, 694, 1161
- Ji, A. P., Frebel, A., & Bromm, V. 2014, *ApJ*, 782, 95
- Keller, S. C., Bessell, M. S., Frebel, A., et al. 2014, *Nature*, 506, 463
- Kitayama, T., Yoshida, N., Susa, H., & Umemura, M. 2004, *ApJ*, 613, 631
- Komiya, Y., Suda, T., & Fujimoto, M. Y. 2015, *ApJ*, 808, L47
- Lai, D. 2000, *ApJ*, 540, 946
- Larson, R. B. 1969, *MNRAS*, 145, 271
- Machacek, M. E., Bryan, G. L., & Abel, T. 2001, *ApJ*, 548, 509
- Mac Low, M.-M. 1999, *ApJ*, 524, 169
- Matsumoto, T., & Hanawa, T. 2003, *ApJ*, 595, 913
- Machida, M. N., Omukai, K., Matsumoto, T., & Inutsuka, S.-I. 2009, *MNRAS*, 399, 1255
- Machida, M. N., & Doi, K. 2013, *MNRAS*, 435, 3283
- Machida, M. N., & Nakamura, T. 2015, *MNRAS*, 448, 1405
- Marassi, S., Chiaki, G., Schneider, R., et al. 2014, *ApJ*, 794, 100
- Mayer, M., & Duschl, W. J. 2005, *MNRAS*, 358, 614
- Nagasawa, M. 1987, *Progress of Theoretical Physics*, 77, 635
- Neufeld, D. A., & Kaufman, M. J. 1993, *ApJ*, 418, 263
- Neufeld, D. A., Lepp, S., & Melnick, G. J. 1995, *ApJS*, 100, 132
- Nozawa, T., Kozasa, T., Umeda, H., Maeda, K., & Nomoto, K. 2003, *ApJ*, 598, 785
- Nozawa, T., Kozasa, T., Habe, A., et al. 2007, *ApJ*, 666, 955
- Nozawa, T., Kozasa, T., & Nomoto, K. 2012, *ApJ*, 756, L35
- Omukai, K. 2000, *ApJ*, 534, 809
- Omukai, K., & Palla, F. 2003, *ApJ*, 589, 677
- Omukai, K., Tsuribe, T., Schneider, R., & Ferrara, A. 2005, *ApJ*, 626, 627
- Omukai, K., Hosokawa, T., & Yoshida, N. 2010, *ApJ*, 722, 1793
- Peebles, P. J. E. 1980, *Research supported by the National Science Foundation. Princeton, N.J., Princeton University Press*, 1980. 435 p.,
- Penston, M. V. 1969, *MNRAS*, 144, 425
- Pollack, J. B., Hollenbach, D., Beckwith, S., et al. 1994, *ApJ*, 421, 615
- Ritter, J. S., Safrank-Shrader, C., Gnat, O., Milosavljević, M., & Bromm, V. 2012, *ApJ*, 761, 56
- Safrank-Shrader, C., Milosavljević, M., & Bromm, V. 2014, *MNRAS*, 438, 1669
- Safrank-Shrader, C., Milosavljević, M., & Bromm, V. 2014, *MNRAS*, 440, L76
- Safrank-Shrader, C., Montgomery, M. H., Milosavljević, M., & Bromm, V. 2016, *MNRAS*, 455, 3288
- Santoro, F., & Shull, J. M. 2006, *ApJ*, 643, 26
- Schady, P., Page, M. J., Oates, S. R., et al. 2010, *MNRAS*, 401, 2773
- Schneider, R., Ferrara, A., Salvaterra, R., Omukai, K., & Bromm, V. 2003, *Nature*, 422, 869
- Schneider, R., Omukai, K., Inoue, A. K., & Ferrara, A. 2006, *MNRAS*, 369, 1437
- Schneider, R., & Omukai, K. 2010, *MNRAS*, 402, 429
- Shu, F. H. 1977, *ApJ*, 214, 488
- Shu, F. H. 1978, *ApJ*, 225, 83
- Smith, B. D., Wise, J. H., O'Shea, B. W., Norman, M. L., & Khochfar, S. 2015, *MNRAS*, 452, 2822
- Springel, V. 2005, *MNRAS*, 364, 1105
- Stacy, A., & Bromm, V. 2014, *ApJ*, 785, 73
- Suda, T., Katsuta, Y., Yamada, S., et al. 2008, *PASJ*, 60, 1159
- Susa, H., Hasegawa, K., & Tominaga, N. 2014, *ApJ*, 792, 32
- Tegmark, M., de Oliveira-Costa, A., Devlin, M. J., et al. 1997, *ApJ*, 474, L77
- Todini, P., & Ferrara, A. 2001, *MNRAS*, 325, 726
- Tominaga, N., Iwamoto, N., & Nomoto, K. 2014, *ApJ*, 785, 98
- Truelove, J. K., Klein, R. I., McKee, C. F., et al. 1997, *ApJ*, 489, L179
- Truelove, J. K., Klein, R. I., McKee, C. F., et al. 1998, *ApJ*, 495, 821
- Turk, M. J., Abel, T., & O'Shea, B. 2009, *Science*, 325, 601
- Tsuribe, T., & Inutsuka, S.-i. 1999, *ApJ*, 523, L155
- Tsuribe, T., & Inutsuka, S.-i. 1999, *ApJ*, 526, 307
- Tsuribe, T., & Omukai, K. 2006, *ApJ*, 642, L61

- Tsuribe, T., & Omukai, K. 2008, *ApJ*, 676, L45
Umeda, H., & Nomoto, K. 2002, *ApJ*, 565, 385
Vorobyov, E. I., & Basu, S. 2010, *ApJ*, 719, 1896
Whalen, D., Abel, T., & Norman, M. L. 2004, *ApJ*, 610,
14
Woosley, S. E., & Weaver, T. A. 1995, *ApJS*, 101, 181
Yahil, A. 1983, *ApJ*, 265, 1047
Yoshida, N., Abel, T., Hernquist, L., & Sugiyama, N. 2003,
ApJ, 592, 645
Yoshida, N., Omukai, K., Hernquist, L., & Abel, T. 2006,
ApJ, 652, 6
Zafar, T., Møller, P., Ledoux, C., et al. 2011, *A&A*, 532,
A51
Zhu, Z., Hartmann, L., Nelson, R. P., & Gammie, C. F.
2012, *ApJ*, 746, 110